Experimental Investigation of the Thermofluid Behaviour
Within a Flat-Plate Solar Collector

Steven Sookdeo

A Thesis

in

The Department

of

Mechanical and Industrial Engineering

Presented in Partial Fulfillment of the Requirements
for the Degree of Master of Applied Science (Mechanical Engineering) at
Concordia University
Montréal, Québec, Canada

October 2008

Library and
Archives Canada

Published Heritage
Branch

395 Wellington Street
Ottawa ON K1A 0N4
Canada

Bibliothèque et
Archives Canada

Direction du
Patrimoine de l'édition

395, rue Wellington
Ottawa ON K1A 0N4
Canada

Canada

ABSTRACT

Experimental Investigation of the Thermofluid Behaviour
Within a Flat-Plate Solar Collector

Steven Sookdeo

Flat-plate solar collectors are used in solar water heating systems to transfer solar energy to water in the form of heat. The research on solar water heating systems is mainly focused on the design and optimization of the overall system with little attention given to study the thermofluid behaviour inside the collector. The collector is a very crucial part of the system as it is where the actual energy conversion talks place. In the present research, the thermofluid behaviour within the tube of a flat-plate solar collector for a forced circulation solar water heating system is experimentally investigated. Particle Image Velocimetry (PIV) was used to measure the velocity field within the collector tube, while thermocouples were used for temperature measurements. The experiments were performed for six flow rates under one unheated and two heated conditions.

The mean velocity profiles for heated and unheated conditions show that the flow behaviour within the collector tube is significantly modified by the heating. With the heat addition, the location of the maximum velocity is in the lower half of the tube, and the magnitudes of mean and turbulent velocities increased with the heat flux. The temperature data indicated the formation of stably stratified layer of water in the upper region of the tube, which reduces the heat transfer rate. The heat transfer analysis showed that free convection is the dominant mode of heat transfer within the flat-plate solar collector.

Acknowledgement

This thesis would not have been possible without the support of many people. I want to express my gratitude to Dr. Kamran Siddiqui for his supervision, guidance, and encouragement. I appreciate all that he has done in helping me develop throughout this experience.

I would like to show my appreciation to Mr. Robert Oliver, Mr. Chris Kowalewski, Mr. Francesco Nudo, and Mr. Gilles Huard for all of their technical support. I would also like to thank the other members of the research group, Shivani Gajusingh, Majid Nabavi, Nasiruddin Shaikh, Mo Wang and Hadi Babaei for their help with the PIV experiments and the Matlab codes.

Finally, I am forever indebted to my parents for their love and encouragement throughout my life. I am also very grateful to my sister and brother.

Table of Contents

List of Figures

List of Tables

List of Symbols

A_C	Collector Surface Area	m^2
C_p	Specific Heat Capacity at Constant Pressure	J/kgK
D	Diameter of the tube	m
E_l	Ekman Number	
F_h	Heat Exchanger Penalty Factor	
F_r	Collector Heat Removal Factor	
F_r'	System Heat Removal Factor	
Gr	Grashof Number	
G_T	Incident Solar Radiation	W/m^2
g	Acceleration Due to Earth's Gravity	m/s^2
h	Characteristic Length	m
i	Angle of Incidence	$Degrees$
K_s	Stratification Coefficient	
k	Thermal Conductivity	W/mK
L	Length of the tube	m
$\dot{m}$	Mass Flow Rate of the Collector Fluid	kg/s
n	Number of Forced Circulation Systems Connected in Series	
n	Index of Refraction	
Nu	Nusselt Number	

p	Angle of Refraction	*Degrees*
Pr	Prandtl Number	
Q_u	Useful Heat Gain	W
q_l	Average Heat Rate per Unit Length	W/m
q_w	Average Heat Flux	W/m^2
r	Radius of the Tube	
Ra	Rayleigh Number	
Re	Reynolds Number	
Ri	Richardson Number	
t	Time	s
T	Temperature	K
T_p	Particle Response Time	s
u	Average Horizontal Velocity	cm/s
$(UA)_x$	Overall Heat Exchanger Conductance	W/K
W	In-Plane Vertical Displacement	μm
w	Vertical Velocity	cm/s
$\overline{w}$	Mean of the Vertical Displacement	μm
Z	Non-Dimensional Axial Length	
z	Axial Location of Measurements	m

Greek Letters

α	Angle Between the Pipe Axis and the Earth's Rotation Axis	*Degrees*
β	Volumetric Thermal Expansion Coefficient	$\frac{1}{K}$
Δ	Difference	
ε_u	Error Due to Velocity Gradient	$\frac{cm}{s}$
ε^2	Variance of the Errors	$\frac{cm^2}{s^2}$
η	Collector Efficiency	
θ	Non-Dimensional Temperature	
μ	Dynamic Viscosity	$\frac{kg}{m \cdot s}$
ν	Kinematic Viscosity	$\frac{m^2}{s}$
ρ	Density	$\frac{kg}{m^3}$
Ω	Angular Velocity of the Earth	$\frac{rad}{s}$
σ_w	Standard Deviation of the Vertical Displacement	μm

Subscripts

1	First Material
2	Second Material
avg	Average

b	Bulk
f	Fluid
i	Inlet
m	Mean
max	Maximum
o	Outlet
p	Particle
w	Water
x	Local

Chapter 1 – Introduction

Energy usage is under increased scrutiny because of its rising cost, depletion of conventional energy sources and damaging environmental effects. One solution to this issue is to use alternative energy sources which are advantageous because they have a lower impact on the environment, reduced operating costs and are sustainable.

The International Energy Agency, in their *World Energy Outlook 2006,* analyzed and projected world energy resources and needs for the period of 2004 to 2030 (International Energy Agency, 2006). In their models, they considered government policies that were in place in 2006; assumed that the population will increase by 1% per year; and that world GPD will grow by 3.4% per year. Their analysis shows that the global primary energy demand will increase by an average of 1.6% per year – a 53% increase between 2004 and 2030. They also presented global supply. At current consumption rates, the proven reserves of conventional energy resources are presented in Table 1.1.

Table 1.1: Proven Reserves of Conventional Energy Resources (International Energy Agency, 2006)

Resource	World's Proven Reserves	Projected Demand Increase [per cent per year]	Years
Coal	909 Billion Tonnes	1.8	164
Oil	1293 Billion Barrels	1.3	42
Natural Gas	180 Trillion Cubic Metres	2	64

Electricity demand is projected to grow by 2.6% per year, with the residential sector having the most rapid growth (International Energy Agency, 2006) due to population growth and economic development around the world. With limited supply, the cost of conventional energy will only increase.

The environmental impact of using fossil fuels for energy is well documented. Their combustion produces many air pollutants: nitrogen oxides, nitrous oxide, sulphur oxides, carbon monoxide, carbon dioxide, volatile organic compounds (VOCs) and suspended particulates (Health Canada, 2004). The presence of these products in the air is damaging to the respiratory system. Some of them are key contributors to smog (nitrogen oxides, nitrous oxide, sulphur oxides, VOCs and particulate matter) and acid rain (sulphur oxides and nitrogen oxides). Carbon dioxide and nitrous oxides are two greenhouse gases. These gases absorb sun's energy and prevent heat from leaving the Earth. They contribute to global climate change.

The entire cycle of extracting these resources from the Earth through to the delivery of energy to the end user significantly damages local ecosystems. Natural habitats disturbed by coal mining or tar sands operations could not revive for decades which impacts the local inhabitants and vegetation considerably. In addition, the water in local lakes and streams becomes contaminated with pollutants endangering the aquatic life.

In order to develop sustainability, the use of fossil fuels has to be more discriminate. Reducing consumption and redesigning infrastructure and buildings can go a long way in mitigating the adverse environmental effects and relaxing the strains on the supply of conventional energy sources. Using other energy technologies is also an important solution. There are alternative energy sources that are being developed and implemented. These sources are renewable: they convert natural occurrences to useful energy in the form of electricity or heat. They include wind energy, tidal power, geothermal energy and solar energy.

Wind energy can be converted into electricity using wind turbines. Installed in areas of high wind energy, the turbine rotates and turns a generator to produce electricity. Individual homeowners can own small turbines to meet their electricity needs. Communities may use large wind farms, which are a collection of wind turbines concentrated in one area. They are located in open, rural areas or offshore. Offshore wind farms are well placed because of consistently high winds and their remoteness from population centres. There are a few issues that must be considered when introducing a wind turbine to the local ecosystem. They cannot be placed near any migratory patterns because birds and bats have been killed by flying into the turbine. Another consideration is the noise produced by the wind turbine which could affect the nearby community.

Water, similarly, is used to turn turbines to generate electricity. The most common application is the hydroelectric dam where river water is directed to spin

3

turbines located in the dam. There are also tidal and damless stations that generate electricity by capturing the energy of the underwater currents. Again, the remoteness of these stations is appreciated by the public. However, they are intrusive to the environment and affect aquatic life.

Geothermal energy uses heat that is stored in the Earth to generate electricity or for heating. At depths underground, there are regions with hot dry rock. By pumping water into these wells to be heated, geothermal power plants use the resulting steam to drive turbines just like conventional power plants. For heating, a working fluid is circulated through a system of pipes buried underground and a heat exchanger is used to capture energy from the warmer ground to dry crops, heat buildings or heat water.

Solar energy uses the sun's radiation for power generation or heating. It is estimated that the solar radiation that hits the Earth in 30 minutes is equal to the world's annual energy demand (Kalogirou, 2004). Another study indicated that the amount of solar energy incident on the Earth is about 15,000 times the energy utilized worldwide (Berman, 2006). This indicates that solar energy can potentially fulfill global energy demand. Solar energy can be used to generate electricity in two ways. First, the sunlight can be used to heat water. At these stations, the sun's radiation is concentrated through the use of mirrors, also called parabolic reflective troughs, which direct the energy to a water-filled pipe located along the focal line of the mirror. The water is continuously heated as it

moves downstream becoming steam which then turns turbines. The second way is by using photovoltaic solar panels. As sunlight hits the solar panel, which is made of a semiconducting material, electrons are freed from their atoms and flow as electric current. Like geothermal energy, solar energy has other uses. It is used to heat air for space heating or crop drying. It can also heat water that is used for domestic consumption such as cooking, bathing, and cleaning.

In 2004, 347.7 PJ of energy was used for residential water heating in Canada (Natural Resources Canada, 2006). It could cost $180 to $480 per year per household (Boone, n.d.). Water heating, which utilizes almost one-quarter of the total energy (Aguilar et al., 2005), is the second largest residential energy consumer. Figure 1.1 shows a breakdown of the residential energy consumption in Canada. Due to the significant energy consumption by water heating, it is one of the areas where there is a tremendous potential for widespread use of alternative energy, specifically the solar energy.
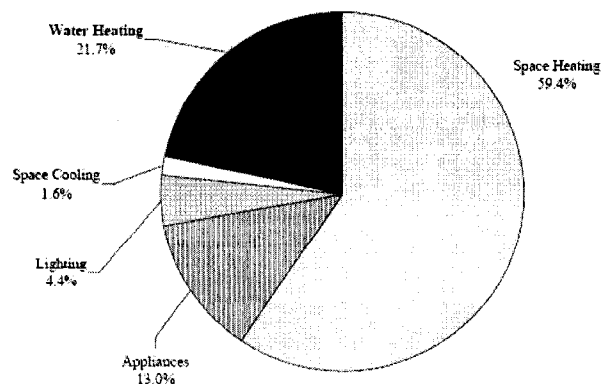
Figure 1.1: Residential energy end use in Canada in 2002 (Aguilar et al., 2005).

Systems that use solar energy for water heating are known as Solar Domestic Hot Water (SDHW) systems. Solar water heating systems are widely used in regions close to the equator. However, in regions closer to the poles like Canada, this technology is limited. The amount of solar energy available may not be enough to meet the water heating needs of the consumers, especially in the winter months. This does not eliminate solar technology as a solution in these areas. Rather, they are used seasonally or in tandem with auxiliary water heaters. In the latter case, the water is pre-heated to an intermediate temperature with solar energy; then, energy from a conventional source, like gas or electricity, heats the water to the desired temperature (typically 60°C). Consequently, there is reduced energy consumption from conventional sources which will reduce the overall energy cost and environmental impact.

Depending on the location and hot water usage, these systems may provide between 1500 and 3000 kWh per year (Natural Resources Canada, 2003). Simulations published by Natural Resources Canada (Figure 1.2) have shown that potential energy savings can be as high as 53% in Medicine Hat, Alberta. The potential savings in Montréal is about 44%.

Figure 1.2: Potential energy savings due to solar water heating systems (Natural Resources Canada, 2003).

The main drawback of these systems is the initial cost. Compared to conventional water heating systems they are more expensive to buy and install, but their lower operating costs make them a viable long-term investment (Boone, n.d.). The long term savings are even more significant as the cost of energy from conventional sources rises. In addition, some governments offer incentives that help reduce the start-up costs for consumers.

1.1 Solar Water Heaters

The main components of solar water heating systems are the solar collector and the storage tank. The solar collector is used to capture the sun's energy that heats the water. It is the part of the system where the actual energy conversion takes place. An insulated tank is used for water storage. Solar domestic water heaters can be described by the way the fluid flows through the collector. In thermosyphonic systems, water moves by natural convection. That is, as the water is heated in the collector, its density decreases causing it to rise and move to the tank that is located above the collector. Cooler, denser water from the bottom of the tank enters the collector to be heated, as shown in Figure 1.3. Water is drawn from the upper portion of the tank which is sent directly to the load or to an auxiliary heater. It is replaced by the incoming cold water which enters the tank near the bottom. The advantage of thermosyphonic systems is that a pump is not required to circulate water through the collector-tank system.
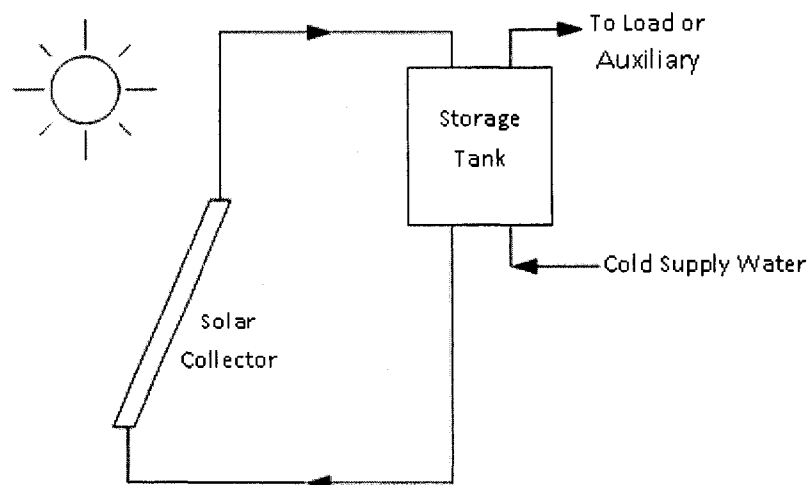
Figure 1.3: Schematic of a thermosyphonic system.

If the water is pumped through the collector, it is called a forced system. A forced system can be further categorized as either direct heating or indirect heating. Direct heating systems have the potable water pumped through the collector. Water is pumped from the bottom of the tank and returns to the tank near the top (see Figure 1.4). This configuration ensures that the cooler water is heated. Heated water is drawn from the top of the tank, while incoming cold water from the mains enters at the bottom. These systems are good where the outdoor temperature remains above freezing.
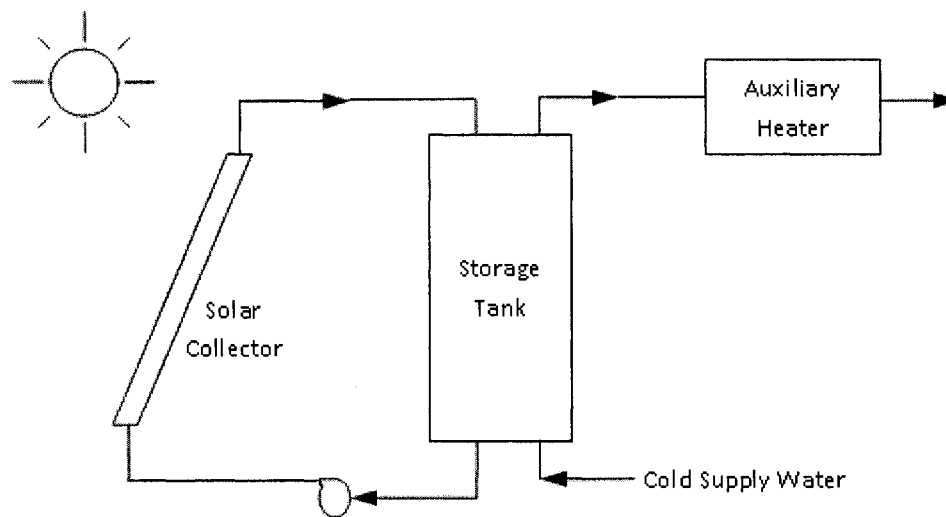
Figure 1.4: Schematic of a direct heating forced system.

Indirect systems pump a working fluid, such as an ethylene-glycol water solution, through the collector. The solar energy heats this secondary fluid which then transfers heat to the potable water through a heat exchanger (see Figure 1.5). The potable water is pumped from the bottom of the storage tank and returns

near the top. These systems are useful when the outdoor temperature drops

below freezing and water cannot be directly heated by the solar collector.
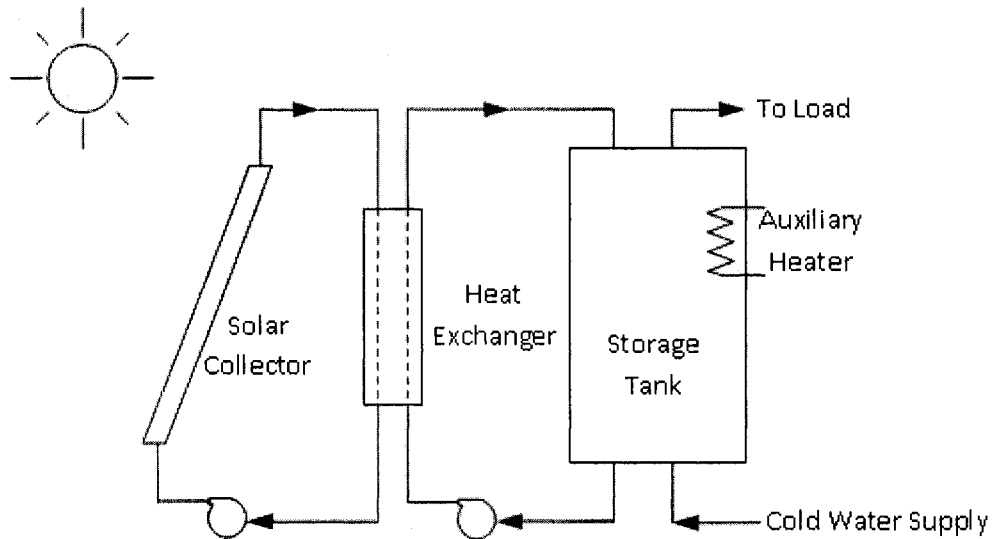
Figure 1.5: Schematic of an indirect heating forced system.

Figures 1.4 and 1.5 also show two ways of auxiliary heating. That is, the water

can be passed to a second storage tank that will heat it to the desired

temperature. Or, an auxiliary heater can be added to the storage tank.

The solar collector for these systems is the flat-plate type. These collectors,

shown in Figures 1.6 and 1.7, are made of an absorber plate, tubes/risers, and a

glazing inside an insulated box. The absorber plate and tubes are made of a

material with high thermal conductivity, like copper or aluminium. They have a

black, highly absorptive coating to maximize the amount of solar radiation

absorbed by the surface. The glazing is the cover; it is made of transparent glass

or plastic. Its role is to allow short wavelength incident solar radiation through;

block long wavelength radiation emitted by the absorber plate; and minimise convection losses from the air trapped inside of the collector. The other sides of the box are insulated to reduce heat losses to the surroundings.
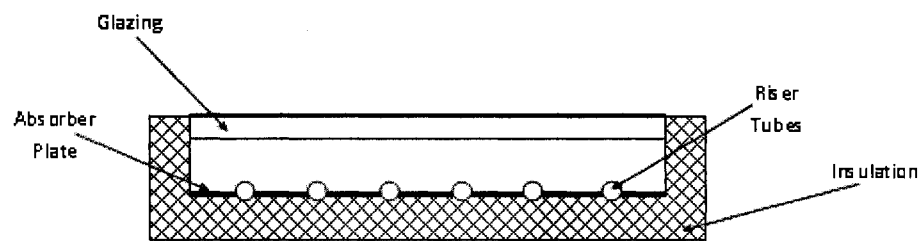
Figure 1.6: Flat plate collector.

The incident solar radiation heats the surface of the absorber plate and tubes. The fluid passing through the riser tubes is at a lower temperature than the surfaces. By conduction and convection, heat is transferred through the absorber plate and tubes to the fluid inside.
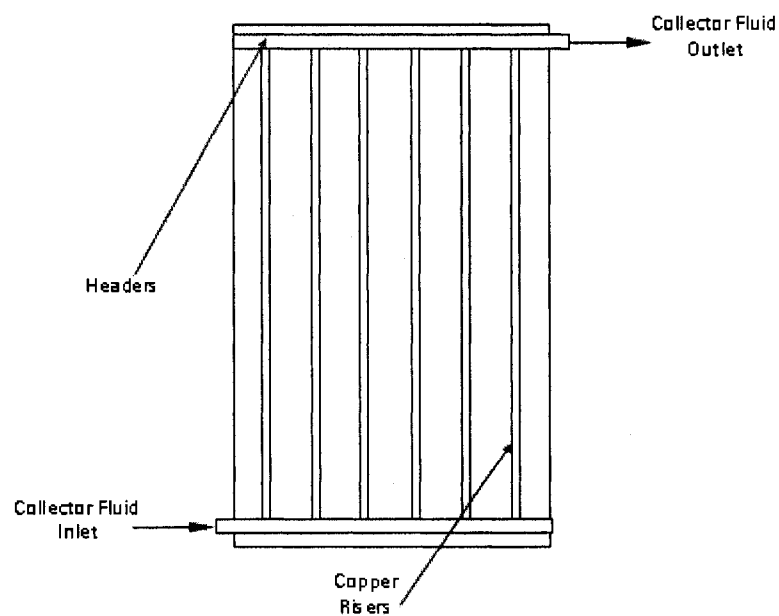
Figure 1.7: Solar collector panel.

11

Some thermosyphonic systems use evacuated tube collectors instead of the flat-plate type. These are made of two concentric glass tubes in which the space between them is a vacuum. The inner tube is coated with a highly absorptive/minimally reflective coating like the absorber plate of the flat-plate collector. The bottom of the tube is closed, while the top is open to the storage tank. Usually, there are many tubes per tank. When there is solar radiation incident on the absorber surface, the water, located inside of the inner tube, is heated and circulates due to natural convection. The warmer water rises along the upper part of the tube and moves towards the tank. Cooler water from the tank, with higher density, enters the tube to be heated. This process is shown schematically in Figure 1.8.
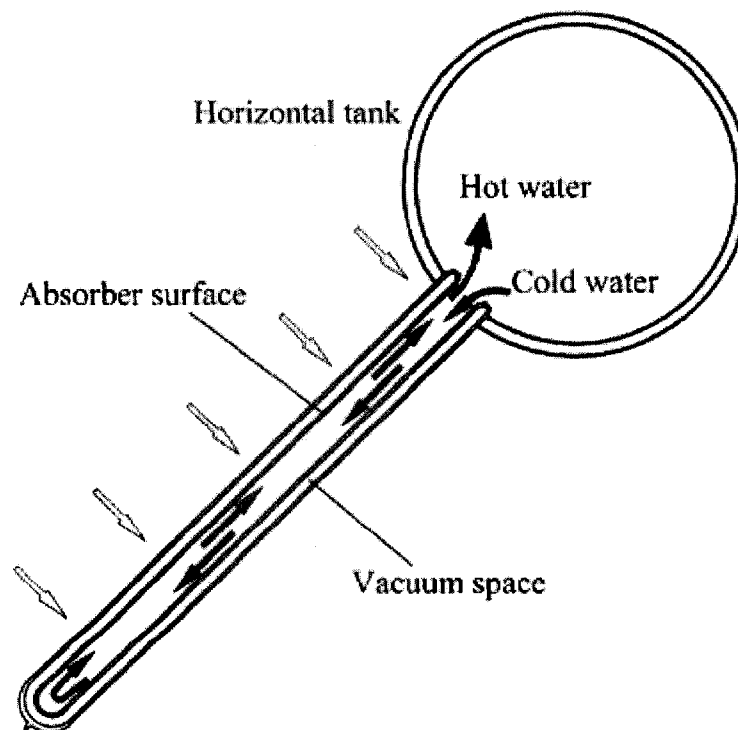
Figure 1.8: Schematic of an evacuated tube collector (Morrison et al., 2005).

Depending on the conditions, evacuated tube collectors may be more efficient than the flat-plate type. Since there is vacuum space between the absorber and the environment, heat is not lost through conduction or convection from the evacuated tube. This is especially advantageous in winter conditions. However, when the difference between temperature of the ambient air and the water at the collector inlet is reduced, flat-plate collectors may perform better. Furthermore, the evacuated tubes are more susceptible for damage and their performance drops significantly if the vacuum is lost. Flat-plate collectors may have two other advantages over evacuated tube types: aesthetics and cost. The first is matter of personal taste, while the latter, described in terms of energy per dollar spent, can greatly influence which type of system is used.

1.2 Literature Review

1.2.1 Collector Flow Rate

The flow rate through the collector influences the collector efficiency and the overall system performance. The efficiency of the collector is given by the following equation (Duffie and Beckman, 2006):

$$\eta = \frac{Q_u}{A_C G_T} = \frac{\dot{m} C_p (T_o - T_i)}{A_C G_T} \qquad (1.1)$$

where η is the collector efficiency, Q_u is the useful heat gain, A_C is the collector surface area, G_T is the incident solar radiation, $\dot{m}$ is the mass flow rate of the

collector fluid, C_p is the specific heat capacity at constant pressure of the collector fluid, T_o is the fluid outlet temperature and T_i is the fluid inlet temperature. As Equation (1.1) shows, the collector efficiency can be improved by increasing the mass flow rate or the fluid temperature difference. For cases where the outlet temperature is specified, the fluid inlet temperature has to be reduced. For a while, high collector flow rates were used because the effect of the flow rate on the system's behaviour was overlooked. However, when considering the overall performance of the system, lower flow rates are advantageous because it permits the water in the storage tank to become stratified. That is, there is little, if any, mixing in the tank; water settles into layers by their density with the lighter, warm fluid at the top and heavy cool fluid at the bottom. The cold water from the mains enters the tank near the bottom. In direct heating systems, the water in the collector loop is withdrawn from the bottom and returns near the top. As a result, the fluid entering the collector is at a low temperature which improves the efficiency. Another benefit is that less energy is "lost" in the mixing of water when the tank is stratified. As well, system costs may decrease because using a lower flow rate would require a less powerful pump and smaller diameter pipes/fittings. In the studies that follow, the optimum performance was found to occur when the flow rate through the collector is equivalent to one storage tank volume per day.

Van Koppen et al. (1979) performed simulations of a pumped direct heating system. They noticed that the energy gain by the system was optimum at a low

14

flow rate. At higher flow rates, the heat gained was lower. They showed that the difference in heat gained by a system with a tank that is stratified compared to one where the water is mixed is greatest at lower flow rates. The difference reduces as the flow rate increases because the stratification is suppressed by the high fluid turnover.

Gordon and Zarmi (1981), through analytical investigation, found that when no hot water is drawn from the tank, the daily efficiency of thermosyphon systems is about the same regardless of the number of passes. A single pass system is described as a system where the entire volume of water in the storage tank passes through the collector once during the day. These systems have lower flow rates compared to multi-pass systems where the water from the tank passes through the collector many times per day. Since the flow rates are higher in multi-pass systems, the increase in temperature per pass is less than that for the single pass system, and hence more passes are required to achieve the same overall water temperature increase. The performance of the two systems varies when the daytime usage is considered. Multi-pass systems deliver more useful energy, but since the water temperature increases incrementally in these systems, auxiliary heat may be required to heat water early in the day, whereas in single pass systems, there may be no need for the additional heat. The suitability of a single pass or multi pass system for a given application depends on its specific load condition.

Robertson and Patera (1982) conducted theoretical analysis of solar water heaters when the output temperature is specified. For fixed inlet temperature, T_i, outlet temperature, T_o, and irradiance, they argued that there is no advantage of using multi-pass systems because the time required to heat the fluid to the outlet temperature is independent of the number of passes. Rather, the increased pump work required makes the overall multi-pass system less efficient.

Phillips and Dave (1982) presented a theoretical model for forced, indirect heating systems. They concluded that the maximum system performance may be achieved with lower collector flow rates. In their analysis, they define the system heat removal factor (F_r') as the product of the collector heat removal factor (F_r: the ratio between the actual rate of heat transfer to the working fluid and the rate of heat transfer at the minimum temperature difference between the absorber and the environment), heat exchanger penalty factor (F_h: the decrease in the collector performance due to the presence of a heat exchanger) and stratification coefficient (K_s: the ratio of actual useful energy gain to the energy gain if there were no thermal stratification in the tank (Phillips, 1981)).

$$F_r' = F_r F_h K_s \qquad (1.2)$$

At high flow rates, F_r increases and K_s decreases. The effect of the stratification coefficient offsets the benefit of F_r. They suggested that high collector flow rates may not be needed because F_r', which should be maximized, is not as sensitive to collector flow rate as F_r.

Jesch and Braun (1984) numerically examined solar water heaters that have variable storage volumes. A variable volume system is one that does not recirculate the water through the collector. This ensures that the collector inlet temperature is always the lowest (the mains temperature) and allows the volume in the storage tank to vary depending on the load. Their results showed that a fixed volume stratified tank, operating at low flow rates, performed the best. Systems that had variable tank volume and variable flow rates were considered a significant improvement over high flow rate systems with no tank stratification but did not perform as well as fixed volume tank systems. They suggested that more work in the design and control of these systems may improve variable volume – variable flow systems.

Joudi and Abd – Alzahra (1984) experimentally investigated a forced system operating at two flow rates and under different load conditions. They found that the system is more efficient when there is a load (water withdrawal) because it results in a lower inlet water temperature to the collector compared to the no load case. An added benefit is that there is less heat loss and subsequently more useful energy transferred to the fluid. They also found that at the higher flow rate, an intermittent load (large volume drawn in a relatively short period of time) had an overall efficiency of 49.5% which is higher than the no load condition (44.1%). For the continuous loading condition, the system was analysed at two different flow rates. They observed an improvement in efficiency of 51.6% and 49.6% for the higher and lower draw off rates, respectively. Additionally, they

observed heat reversal which means that heat was leaving the tank and going to the collector. To manage this, they used a thermostat that was dependent on the temperature difference between the collector and the tank to control the pump. They found that the water in the tank reaches a higher temperature without the thermostat in operation.

Morrison and Braun (1985) simulated a thermosyphon system. They found that the optimum system performance is achieved when the ratio of the daily volume that flows through the collector to the daily load volume is approximately one. They noted that forced circulation systems perform similar to the thermosyphon systems under these conditions.

Wuestling et al. (1985) showed that the annual system performance improves from 11.5% to 14.7% when they are operated at low flow rates and have stratified tanks. Similar to Jesch and Braun (1984) when variable flow strategies are employed, there is an improvement of 9.5% over the conventional systems, but not as much as low flow systems with tank stratification. They found that the optimum system performance is achieved when the monthly-averaged daily total collector flow rate was equal to the daily total load.

Furbo and Mikkelson (1987) compared the performance of three systems under the same conditions (irradiance and consumption of hot water). The three systems included a reference system that was a pumped, indirect system with

the heat exchanger in the bottom of the storage tank; a thermosyphonic system; and a direct heating system with a low flow rate. Their results showed that the pumped low flow system performed 20% better compared to the reference system and 10% better than the thermosyphonic system when the fluid enters the storage tank from the top. They attributed the benefits to stratification in the storage tank.

Lawaetz and Nielsen (1987) simulated two solar water heating systems. The first (conventional) was an indirect heating type with the heat exchanger in the bottom 1/5 of the storage tank and a heater in the top 1/5. The second system, which had a low flow rate, was also an indirect system, but had the heat exchanger in the bottom 4/5 of the tank (the water flowed from the bottom to the top) and a heater in the top 1/5. The conventional system showed performance that is independent of flow rate at high flow rates, while an optimum performance was found for the second system. Comparing the two configurations, the conventional system at a flow rate of 1.0 l/min per m^2 of collector area performed similar to the second system with a flow rate of 0.15 l/min per m^2 of collector area.

Fanney and Klein (1988) compared the effect of flow rate on direct and indirect systems through experimental investigations. They used identical solar water heating systems and showed that the reduction of collector flow rates improve system performance significantly. They also examined the use of tank stratification enhancing return tubes (the tubes that the flow from the collector

enters the storage tank through). Standard return tubes ensure that the flow enters at a specified depth in a single axial flow stream. The stratification enhancing return tubes have regularly spaced holes that redirect the downward flow into numerous radial streams. In their long term test of direct systems, they observed 17% increase in solar energy delivered to the tank, 37% decrease in auxiliary energy consumption, and a reduction of parasitic energy by 17% when the lower flow rate (for tank stratification) was used. The collector flow to load flow ratio was 1.3. They observed that a low flow-rate system with a standard return tube performs slightly better than system with the stratification enhancing tube at standard flow rate. In systems with stratification enhancing return tubes, a reduced flow rate performs better. They measured a 6% increase in the collected solar energy. The also measured the effect of the heat exchanger flow rate used in indirect systems and showed that lowering it did not improve the system performance.

Carvlho et al. (1988) experimentally compared three identical systems under different operating strategies. They examined single-pass, multi-pass and thermosyphonic systems. It is important to note that they had modified the single-pass system to ensure that there was no storage tank mixing. For this system, an equivalent amount of water per day was drawn from an additional tank and passed through the collector. They found that the single-pass system delivered more energy than the multi-pass system. As the available radiation decreased, they found that the difference in thermal performance between these two

increased. They also found that the thermosyphonic system performed slightly better than the multi-pass system but not as good as the single-pass system. They suggest that the modification that they made for the single-pass system would be a good strategy for large systems, but thermosyphonic systems, upon considering the economics and energy usage, are adequate for smaller domestic systems.

Fahmy and Abd – El Sadek (1990) developed a model of a pumped solar water heating system that considers heat loss through the storage tank, as well as the variation in solar radiation, ambient air temperature and cold water temperature. They specifically examined three cases: no heat exchangers (Case 1); heat exchanger in the withdrawal loop and placed inside of the tank (Case 2); heat exchanger in the collector loop and placed inside of the tank (Case 3). For the first and second cases, they found that increases in the withdrawal flow rate increased the efficiency but lowered the outlet water temperature when the collector flow rate is held constant. When the withdrawal flow rate is held constant, increases in the collector flow rate resulted in higher outlet water temperature and higher efficiency. For Case 3, they observed that the increase in the collector flow rate increased the outlet water temperature and efficiency, whereas the increase in the withdrawal rate resulted in lower outlet water temperature but higher efficiency.

Antonopolous and Rogdakis (1991) used the finite difference method to estimate the optimum collector flow rate for one tank forced systems. They simulated the system and predicted the performance over a range of values for a number of parameters (collector characteristics and area; load profile; collector and load mass flow rates; volume of storage tank per unit collector area; thermal loss coefficient of the storage tank; temperature of mains cold water; and weather conditions). They observed that the optimum ratio of collector to mean load mass flow rate ranged between 0.4 and 1.4. They showed that this correlation can be expressed in terms of the ratio of mean load mass flow rate to collector area providing a simple and quick method to determine the optimum collector flow rate.

Hollands and Brunger (1992) studied systems with counterflow exchangers. Unlike the system used by Fanney and Klein (1988) where the overall heat exchanger conductance, $(UA)_x$, was increasing with flow rate, they analysed a system where $(UA)_x$ was constant. Using this premise, they provided a design strategy that can be used to find the optimum collector and exchanger flow rates.

Furbo et al. (2005) measured the thermal performance of a solar water heating system over two years. The system had a total collector area of 336 m^2 and a 10000 L storage tank. It was an indirect heating system with an antifreeze solution passing through the collector that was installed to supply hot water to 425 apartments and a laundry in Sundparken, Elsinore, Denmark. In the two

year period, the average daily consumption was 98 L and 94 L which correspond to 4.9 kWh and 4.7 kWh per apartment per day, respectively. As expected, consumption varied according to the seasons. The yearly net utilized solar energy was 366 and 455 kWh per m^2 of solar collector area for the first and second years, respectively; the yearly solar fraction was 8% and 10%, respectively. Their system compared favourably to other large systems in Denmark. They attributed the good system performance and solar radiation utilization to the high hot water consumption and good system design. They recommended that future large solar heating systems are designed as low-flow with the external exchangers and stratification enhancing inlet pipes.

1.2.2 Forced Systems

Sodha et al. (1982a) examined a forced circulation heating system under two withdrawal cases: constant flow rate and constant hot water temperature. They used a system with and without a heat exchanger placed in the outlet water loop. They showed that the efficiency increases with the outlet water flow rate, but the mean tank water temperature decreases. Furthermore, there were no gains in the outlet water temperature whether or not the heat exchanger was used. They suggested that the heat exchanger should not be used unless its surface area is very long or is necessary because an anti-freeze fluid is used in the collector. Their results showed that the outlet flow rate needs to be controlled in order to obtain hot water at a constant temperature.

Sodha et al. (1982b) analysed a forced system with a heat exchanger in the collector loop under two withdrawal cases: constant flow rate and constant hot water temperature. They showed that the overall efficiency and tank outlet water temperature can be increased, although not substantially, if the collector flow rate is increased. The overall efficiency of the system can also be increased by increasing the hot water withdrawal rate because that will lower the mean storage tank temperature and, subsequently, thermal losses.

Shukla and Tiwari (1983) performed transient analysis of a forced system with n–collectors in series. They considered two withdrawal cases: constant flow rate and constant hot water temperature. They concluded that more than five collectors are not useful for flow rates on the order of 10 kg/hr because of the additional heat loss. They also reported that the hourly variation of the outlet water temperature is affected by the flow rate and retrieval period. They suggested the use of greater number of collectors to meet higher water demands at elevated temperatures. However, in both withdrawal cases, the overall efficiency of the system decreases with the increase in the number of collectors.

Sodha et al. (1983) analyzed a water heating system with n identical forced circulation systems connected in series for the case when the water was withdrawn at a constant flow rate. They concluded that the optimal number of systems to get the maximum water temperature is 3 or 4. They showed that when the number of connected systems is held constant, an increase in the

outlet flow rate causes a gradual decrease in the water temperature. The overall system efficiency increased with the number of systems used until n = 3. They also found that the amount of heat that the system receives increased with the increase in the number of connected systems.

Yadav and Tiwari (1988) conducted a parametric study of the performance of a heat exchanger coupled to a panel of flat plate collectors. They considered a double-pipe exchanger where the hot fluid from the collectors flowed in the outer pipe and the cold fluid from the supply source flowed in the inner tube. They compared the counterflow and parallel flow modes and showed that the counterflow performed better. They also showed that increasing in the length of the heat exchanger or the tube's inner diameter increases the outlet temperature. They also argued that the heat exchanger performance can be improved if the fluid with a high thermal conductivity is used in the inner tube.

Sinha and Tiwari (1992) theoretically examined a commercial system that delivers hot water at a constant temperature using an iterative method. They concluded that the length of the heat exchanger has a significant influence on the mass flow rate. As the length increases, the mass flow rate must increase in order to maintain a constant delivery temperature. They also showed that the mass flow rate would have to change with the time of day, but the flow rate is not very dependent on the number of collectors used in series. According to their

results, the system's overall efficiency decreases with the number of collector panels but increases with the length of the heat exchanger.

Bojic et al. (2002) simulated a solar water heating system using a time marching model. They considered an indirect heating system with the heat exchanger in the collector loop placed inside of the storage tank. Their results showed that the size of the storage tank influences the solar fraction, which increases as the storage tank size increases until an asymptotic value that depends on the required water temperature. They also observed that the solar fraction is slightly lower for cases with the variable load profile compared to the constant load profile.

Hobbi (2007) designed and fabricated a flat-plate solar collector that was used to investigate the use of heat transfer enhancing devices. Specifically, three types of tube inserts were examined: a twisted strip used to induce swirl; a coil-spring to induce swirl and turbulence; and conically shaped ridges (diverging nozzles) used to generate longitudinal vortices. Under the same heating and flow conditions, these devices did not produce significant improvements to the heat transfer to the collector fluid, signifying that free convection is the dominant mode of heat transfer and that the thermal stratification suppresses the turbulence induced by the mean shear. In addition, using the TRNSYS simulation program, the applicability of solar domestic water heaters for a single family residential unit in Montréal was studied. The results showed that a system could provide 85% to

100% of the hot water demand in the summer and 30% to 40% of the demand in the winter.

1.2.3 Evacuated Tube Thermosyphon Systems

Due to the widespread use of evacuated tube thermosyphonic solar water heaters, significant research has been done to study and improve their performance. In the following, a summary of research that is relevant to the study of the flow characteristics in thermosyphonic systems is presented.

Morrison and Ranatunga (1980) used Laser Doppler Anemometry (LDA) to measure the flow rate in a thermosyphon solar collector. They showed that the equations that were accepted at that time to predict the flow rate in thermosyphon systems were inadequate because they underestimated (Reynolds numbers less than 300) and overestimated (high Reynolds number) the flow rate. Specifically, they pointed out that the accuracy of the correlations could be improved by considering friction effects in the developing regions of the flow.

Gaa et al. (1996) used LDA to study the velocity behaviour in inclined open thermosyphon systems. From the experimentally obtained axial velocity profiles, they showed two distinct flow zones – a bifilamental profile. At the bottom of the cross-section, the water flows down towards the closed end, and at the top,

warmer water flows up towards the open end, and the tank. There is with a naturally occurring boundary between the two streams.

Behnia and Morrison (1996) used rheoscopic tracing particles to study the flow pattern and temperature variation in a thermosyphon system. They examined a situation when the bottom half of the tube was heated at a higher rate than the top, which is similar to what is found in evacuated tube solar water heating systems, for three different tube inclinations. To achieve the differential heating, the tube was immersed in a water jacket that was partitioned so that the top half of the tube was surrounded by water at a lower temperature than the water surrounding the bottom half. They defined the heating condition by considering the temperature difference between the fluid in the reservoir (storage tank) and the fluids in the water jacket. Unlike the uniformly heated condition where there was a stagnant region, they observed density induced circulations, which they termed a multi-cellular region, located at the closed end of the tube when bottom of the tube was heated more than the top. The length of this region increased with tube inclination and as the temperature difference between the reservoir and the fluid in the lower partition increased (greater heating differential). When the top half of the tube was heated higher than the bottom half, they did not observe a stagnant or multi-cellular region at the closed end. Rather the water was heated throughout the tube length.

Morrison et al. (2004) used a numerical model to study axial velocity contours in the tube. They describe the flow as bifilamental. That is, there is a cooler layer of water in the bottom part of the tubes cross-section that descends to the closed end and a warmer layer of water in the upper portion of the cross-section that returns the water to the storage tank. When there was uniform heating on the tube wall, they observed a stagnant region near the closed end dependent on the Rayleigh number and aspect ratio. This region of inactivity was not seen when the heat flux on the tube wall was variable.

Morrison et al. (2005) compared the results of a CFD model with the results from Particle Image Velocimetry (PIV) experiments of a water-in-glass evacuated tube solar collector. Both results showed that when the top of the tube is heated, the flow becomes bifilamental. Fluid in the top section of the tube cross-section is warmer and flows back to the tank. The cold fluid from the tank flows in the bottom part of the tube. The numerical and experimental results correlated well. There was a discrepancy near the bottom of the tube where the numerical results predicted a definite peak that was not as pronounced in the experimental results. Also, the PIV seeding limited the number of data points along the tube radius so that, while the PIV experiments showed a triangular velocity profile in the top part of the tube, the CFD showed a parabolic shape. At the opening of the tube, they found that the CFD and PIV results agreed well. Using the CFD model, they examined the effect of the circumferential heat distribution. The simulations showed that as the distribution of heat moved from the bottom of the tube to the

top, the flow rate increased. Compared to the extreme top heating, the flow rate at the uniform heating condition was reduced slightly. The reduction in flow rate when there is extreme bottom heating is more pronounced: it was nearly half. When there is extreme top heating, the proportion of the tube cross-section at ¾ length occupied by the hot and cold streams were similar. With extreme bottom heating, most of the cross-section was taken up by the top, warmer stream.

1.2.4 Heat Transfer in Tubes with Longitudinal Fins

The flat-plate collector can be modelled as a tube with two external longitudinal fins having solar radiation incident on the upper surface of the tube and fins. However, there is scarcity of studies on the flow behaviour within such geometry.

Barozzi et al. (1985) experimentally investigated mixed convection in horizontal and inclined tubes. Under axially uniform wall heat flux and laminar flow conditions for a horizontal pipe, they observed that the local Nusselt number (Nu_x) decreased from high values at the inlet to a minimum at a downstream location and then to an asymptotic condition further downstream. They attribute the rapid decrease at the inlet to entrance effects which are in balance with the free convection effects at the location where the minimum local Nusselt number occurs. They also found that the mean Nusselt number (Nu_m) decreased with downstream location. They performed one experimental set at high heat flux and relatively low flow rates. The resulting behaviour was very different: downstream,

there was not any asymptotic behaviour. Flow rates at Reynolds numbers in the transition region behaved quite differently. The local Nusselt number at the entrance was very high and decreased to a minimum, the downstream trend is not asymptotic but increasing. They suggested that Reynolds number, Prandtl number and Rayleigh or Grashof number have independent effects on the heat transfer rate for these cases. When the pipe was inclined and there was ascending laminar flow, they found that the mean Nusselt number decreased as the flow moved downstream. As the tube inclination angle increased, they found that there were slight decreases in the mean Nusselt number. The variation in Nu_m with inclination angle decreased with increasing Reynolds number. They suggested that the influence of the inclination angle can be disregarded for practical applications.

Ouzzane and Galanis (2001) numerically analysed heat transfer in a tube with a longitudinal fin. This system is modelled as a flat-plate collector. The heat flux (solar radiation) was incident on the top surface. The bottom surface was insulated. Their results showed that most of the energy is conducted to the fluid in the bottom half of the tube. They observed that, far downstream, the top half behaves as if it was under an isothermal condition. Also, the secondary flow, caused by natural convection, is symmetric about the vertical axis. The fluid near the tube wall is heated and rises along the wall. The fluid near the centre plane is cooler, causing it to move towards the bottom. These eddies become stronger as the fluid moves downstream until a maximum intensity is reached. After

which, the intensity decreases until the fully developed condition is achieved. They found that the axial velocity distribution was symmetric at the entrance. Downstream, the buoyancy effects of the natural convection became pronounced causing the axial velocity profile to no be longer symmetric; i.e. it is a distorted parabolic shape. The maximum velocity occurs in the top half. The flow velocity increased along the length of the tube. Finally, they showed that the thermal performance decreased as the width of the fins increased when the collector's dimensions were held constant.

1.2.5 Non-Uniform Heating

Horizontal tubes under non-uniform heating have been studied under two heating conditions – heating from below and heating from above. Only the latter case is reviewed since it relates to flat-plate collectors.

Patankar et al. (1978) numerically investigated a tube in which the top half was heated and the bottom half was insulated. They showed that there was a tendency for the flow to be stratified. The degree of stratification increased with the modified Grashof Number Gr^*. They found that, as Gr^* increased, the secondary flow profile became an increasingly distorted "kidney bean" shape. They found that when $(2/\pi)Gr^*$ was 10^6, there were four eddies in the cross section.

Ouzzane and Galanis (1999) numerically investigated convection in inclined tubes heated in the top half with an adiabatic bottom. Their results showed that all of the heat is supplied to the fluid in the top half of the tube at the entrance. With an increase in the downstream distance, the heat started to reach the bottom through wall conduction. They note that further downstream, more heat is supplied to the fluid in the bottom than in the top. As buoyancy effects become more prominent, the location where the fraction of heat supplied to the fluid in the bottom is equal to the fraction supplied to the fluid in top moves upstream rapidly. There is a Grashof number, in their case $Gr = 2 \times 10^5$, where this location starts to gradually move downstream. They found that the counter-rotating eddies are more intense at larger values of the Grashof number. The eddy intensity evolved along the tube length becoming more intense until a peak was met and then, decreased until it reached the fully developed state. They presented the velocity profiles for three different Grashof numbers ($Gr = 0$, 10^5, 10^6). For all cases, they found that the maximum velocity occurs far downstream. However, the peak of the distorted parabola for the $Gr = 10^5$ case is in the bottom half of the tube, while it shifts to the top half for the larger Grashof number ($Gr = 10^6$).

1.3 Motivation

The majority of the previous studies on solar collectors were focused on evaluating and analyzing their overall performance and, specifically, the thermosyphon-type of collectors. The flow behaviour inside the collector fluid has

not been investigated in detail and thus, it is poorly understood. The thermofluid interactions inside of the collector tube are complex. The heat flux to the water inside is circumferentially non-uniform. Through circumferential conduction, most of the heat flux reaches the water from the bottom part of the tube. This results in buoyancy induced secondary flow where heat is transferred within the fluid through natural convection. Thus, the overall heat transfer inside the collector tube is mixed convection. To improve the performance of flat plate collectors, it is desired to improve the heat transfer. However, a previous study has shown that the conventional mixing strategies used to enhance the heat transfer do not work in flat-plate solar collectors (Hobbi, 2007). It is vital to understand the flow behaviour inside the collector tube and then use this information to develop techniques to enhance the heat transfer inside the collector tube. This would improve the thermal performance of solar collectors making them more feasible for cold regions like Canada.

1.4 Objectives

The objective of this research project is to investigate the thermofluid behaviour inside the flat-plate collector used in solar domestic water heating systems. The results from this study would provide better insight into the flow structure inside collector tube. This will allow researchers to develop improved numerical models and heat transfer enhancement strategies. This will eventually lead to the development of more efficient solar water heating systems.

1.5 Thesis Layout

This thesis is organized into four chapters. In Chapter 1, the main types of solar water heaters are described after detailing the potential of solar energy for water heating. It includes a literature review consisting of work relating to the collector flow rate; forced and evacuated tube solar water heating systems; heat transfer in tubes with longitudinal fins; and heat transfer in tubes that are non-uniformly heated from above. The motivation and objectives of this work conclude Chapter 1. Chapter 2 describes the experimental apparatus and procedure. It outlines the PIV measurement technique and the image processing method. The results of the experiments are presented in Chapter 3. Specifically, the mean velocity profiles and collector tube temperatures are interpreted with heat transfer parameters and turbulent velocity characteristics to describe and characterize the physical phenomenon occurring within the collector tube. Chapter 4 summarizes these results and recommends future work that can be researched.

Chapter 2 – Experimental Setup and Technique

2.1 Experimental Apparatus

The main experimental apparatus used in this study was designed by Mr. A. Hobbi as part of his Master's thesis (Hobbi, 2007). It was modified for the present work. The schematic of the apparatus is shown in Figure 2.1. In real applications, the collector tubes are inclined. However, due to experimental challenges, it was not possible to consider the inclined tube in the present study. The different components of the apparatus are described in detail in the following.
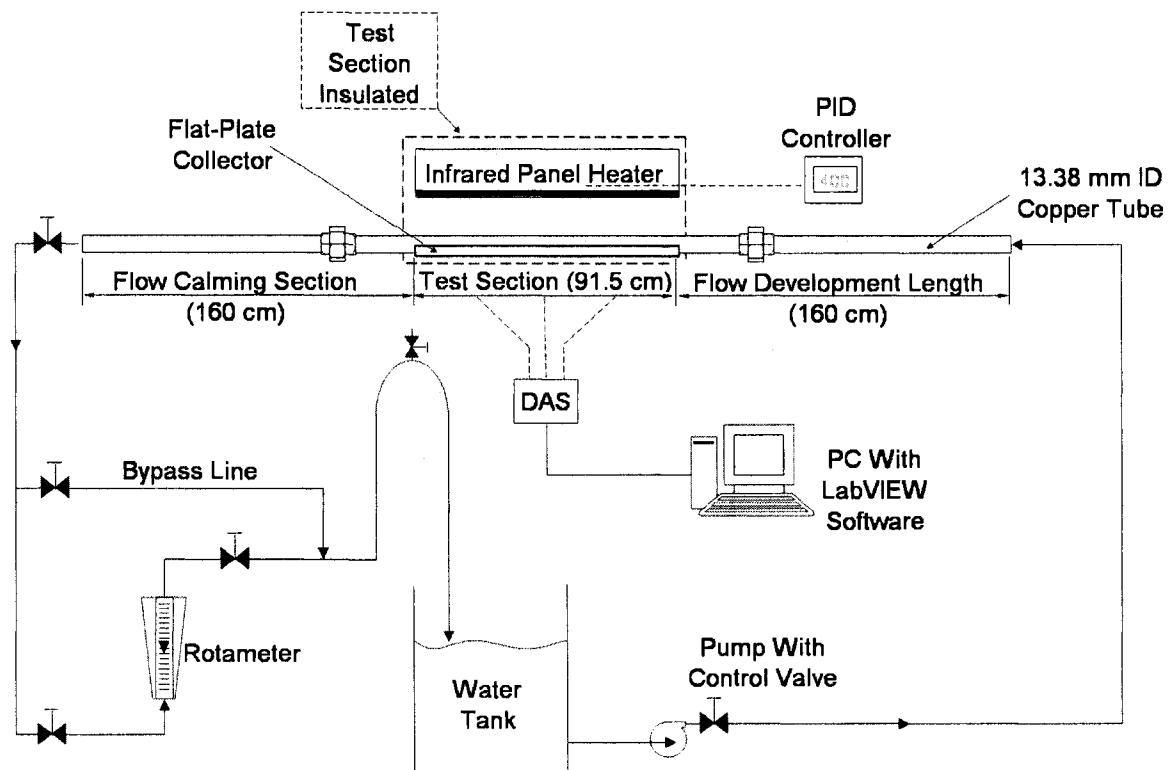

Figure 2.1: Schematic of the setup.

The flat-plate collector was made of ½ inch Type K copper pipe (13.38 mm diameter, 1.24 mm wall thickness) soldered onto a copper plate that was 915 mm × 152 mm × 1.1 mm (see Figure 2.2). The plate area was 0.145 m^2.

Test Section
Insulated All
Around

Panel Heater

Flat-Plate
Collector

50 mm
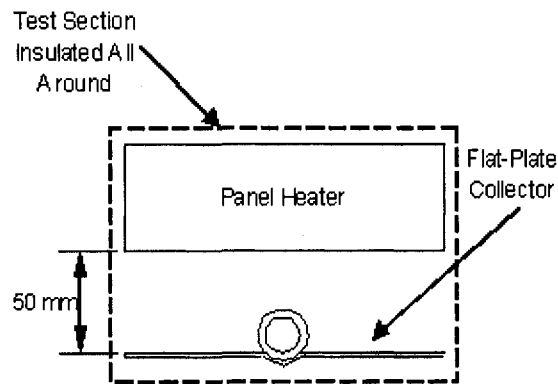
Figure 2.2: Front view of the test section.

The pipe and plate of the collector were painted with black, high temperature paint (Tremclad High Heat Enamel). The upstream end of the collector was connected to a ½ inch 1.6 m long copper tube to ensure that the flow was fully developed at the collector's entrance (see Figure 2.1). A similar copper tube of the same length was attached at the downstream end of the collector to allow the flow to settle down. The flow rate was controlled by a rotameter (Omega Engineering, Model FL–1448–G) connected downstream of the collector. The range of the rotameter is 4.5 to 577 ccm.

The present work is focused on the velocity measurements inside the tube using the Particle Image Velocimetry (PIV) technique. This method, described in Section 2.2, requires optical access into the tube to remotely measure the velocity field. For this purpose, the apparatus was modified to fit a transparent glass window to allow optical access. Pyrex glass test tubes of 15.8 mm outer

37

diameter and 14.3 mm inner diameter were cut into the lengths of 50 mm and inserted at the measurement locations. The inner diameter of the glass tube was 6.7% larger than the inner diameter of the copper pipe; however, the influence of this change in flow area is insignificant compared to the effect of the heating. To mitigate the optical distortion due to the curvature of the glass tube, a water-filled acrylic box was constructed and to surround the glass tube at the measurement section. This is described in Section 2.3.

A high temperature infrared panel heater (Omega QF-063610-T) supplied thermal energy to the collector through radiation. The maximum heater density is 15500 W/m^2 and the wavelength of the output thermal radiation is between 2.5 and 6 microns. Although the heater cannot cover the radiation spectrum of solar energy, the radiant heat flux from the heater was within the acceptable range. The face of the heater was black quartz-ceramic cloth and was installed 50 mm above the collector (see Figure 2.2). The surface dimensions of the radiant heater were same as that of the collector (i.e. 915 × 152 mm).

The temperatures of water and collector surface were measured via type K thermocouples. The water temperature was measured at the inlet and exit of the collector to quantify the heat transferred to water. The inlet temperature was also used to verify that the temperature of the water entering the collector remained almost constant during each experiment. The wall surface temperature of the collector tube was measured at nine different locations as shown in Figure 2.3.

Three circumferential temperatures, the top of the tube; bottom of the tube; and the joint of the tube and plate, were measured at the inlet, middle and outlet of the tube. The temperatures were recorded using a National Instruments (NI SCX-1000) data acquisition system with a 16 channel card (PCI-6063-E). The data was acquired using the LabVIEW 7 Express software. The sampling rate was 100 Hz. The system was enclosed with Reflectix R-4 thermal insulation with reflective surfaces as shown in Figure 2.4. In addition to minimizing thermal losses, it also helped protect the camera used in the PIV measurements from the heat.
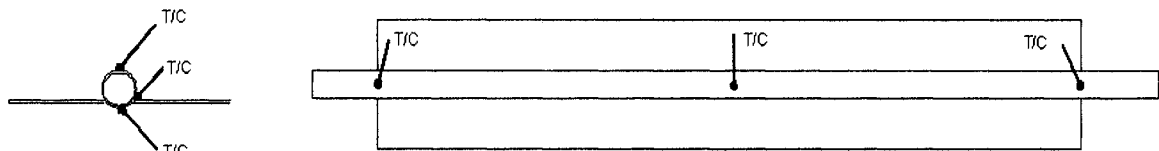

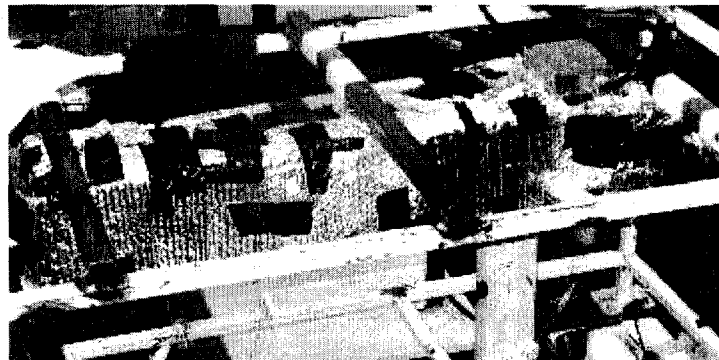Figure 2.3: Location of the thermocouples on the collector tube.

Figure 2.4: Flat-plate collector and heater enclosed in the insulation.

Hobbi (2007) used city water directly from the tap for his experiments. A new source had to be found for the PIV measurements because air bubbles in the city water had a tendency to stick to the inner wall of the glass. Even though the

bubble size is very small relative to the test section, they cover a considerable area and reduce the optical access to the measurement region resulting in very poor quality images. Two solutions were considered. One was to use distilled water. The second was to use tap water that was allowed to settle in a reservoir for at least 24 hours prior to the experiments so that the air bubbles would be removed from the water. The latter option was successfully tried and then used for all of the experiments. The water was stored in a tank of size 46 cm × 46 cm × 64 cm (outer dimensions, wall thickness 6 mm). A large volume of water was used to ensure that the temperature did not vary significantly during the experiments. As an additional preventative measure, the glass tubes were washed with diluted hydrochloric acid to clean any residual impurities on the surfaces.

Water was circulated through the collector by a magnetic pump (Little Giant Pump Company, Model 4-MD). A valve was installed at the pump outlet to help control the bulk flow rate. The precise flow rate for a given case was adjusted through the rotameter.

2.2 PIV Technique

2.2.1 Introduction to PIV

Particle image velocimetry (PIV) is a nonintrusive optical technique used to measure flow velocities. A typical PIV system consists of a laser as the light source, a camera to capture the images, a PC equipped with a frame grabber to record and store the images, and a delay generator to control the timing of the laser pulses with respect to the camera frames. In this technique, the flow is seeded with neutrally or near-neutrally buoyant tracer particles that follow the flow. A pulsed laser light sheet illuminates a plane in the flow causing the tracer particles to glow. The camera records the image of the particles which shows their position at that instant of time (t). A short time later (Δt), a second pulse illuminates the same plane creating a second image of the particles showing their position of the particles at the second instant of time (t + Δt). In this way, a series of image pairs are obtained. Each image pair is then processed to compute the displacement of the particles between the first and second images of the image pair. The velocity field is obtained by dividing the particle displacement by the time difference (Δt) between the two images of the image pair.

A more detailed description of the velocity field computation by PIV image pairs is described as follows. The first image of the image pair is divided into small regions called the interrogation windows such that the velocity of particles in this region is approximately uniform. In the present study, the size of each interrogation window was set equal to 32 × 32 pixels. The second image is

41

divided into relatively larger regions called the search windows. The dimensions of the search window are typically set to twice the dimensions of the interrogation window so that the particles in the interrogation window of the first image can be found within the corresponding search window in the second image. The size of the search window in the present study was set equal to 64 × 64 pixels. Cross-correlation between the interrogation region in the first image and the search region in the second image is performed and the maximum of the cross-correlation function gives the average particle displacement within that interrogation region. The cross-correlation operation is performed on all interrogation windows in the given image pair to obtain the velocity field over the entire image. A sample of these images is displayed in Figure 2.5.
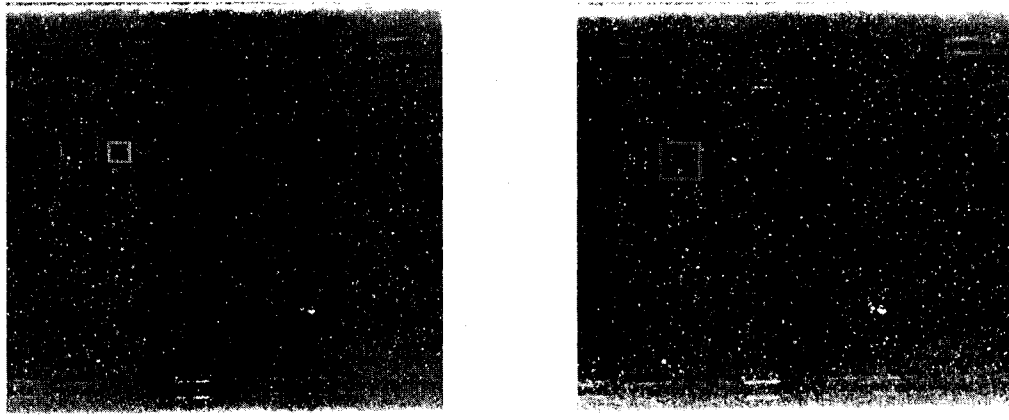

Figure 2.5: An image pair showing an interrogation region (left) and the corresponding search region (right). The size of each interrogation region is 32 × 32 pixels and the size of each search region is 64 × 64 pixels.

The particle shift between the two images of an image pair depends on the time interval (Δt) between the two images. Since the particle velocity for each

experimental run varied, the time interval between the two images of the image pair was adjusted for each flow rate to maintain a good particle shift.

Due to unavoidable particle accumulation and air bubbles on the glass tube wall, the optical access to the measurement region was poor in some regions. As a result, several velocity vectors computed in these regions were spurious. However, one favourable aspect was that the position of accumulated particles and air bubbles on the glass tube wall was constant during a particular experimental run. Therefore, these regions and the corresponding spurious vectors could be readily isolated from further analyses. For this purpose, each set of images was examined to find any consistent sources of discrepancies (particle accumulation, reflections and air bubbles). A binary threshold image of the same dimensions as the original image was created for each run, where the regions with low or bad optical access were marked. A typical binary threshold image is shown in Figure 2.6. In the image "1s" (white regions) correspond to the regions with bad quality of particle images and "0s" (black regions) correspond to the regions with good quality of particle images.
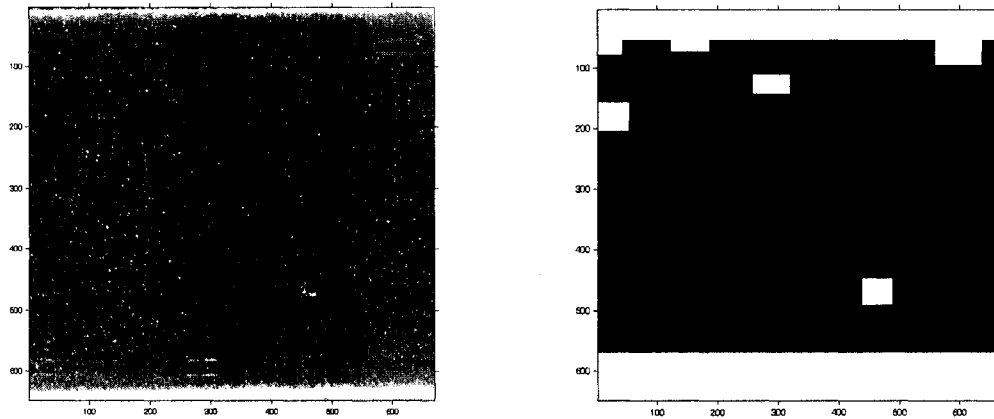
Figure 2.6: Original PIV image (left) and the corresponding Binary Threshold Image (right). The particle accumulation on the top and bottom walls, as well as some reflections and air bubbles are clearly visible in the PIV image.

A Matlab code was used to find and correct any spurious vectors in the good region using a local medial test (Siddiqui et al., 2001). The code was modified to consider the bad regions from the binary threshold image (white areas) and exclude the velocity data in these regions from further analyses. In the modified code, the parts of the data that corresponds to white areas on the threshold images are replaced with *NaN* (Not-A-Number). These data points are ignored in the rest of the code. Each velocity vector (magnitude and direction) is then compared with the median of its eight neighbouring vectors. Note that if *NaN* is one of the neighbours, then it is not considered in the median test. If the magnitude and direction of the given velocity vector is outside a pre-determined range, it is replaced by the median of its neighbours. Finally, the code converts the values of each vector from pixels to cm/s. The conversion factor was determined by taking an image of a ruler that is inserted into the test section under experimental conditions and measuring the number of pixels between

44

graduations. An example of a velocity field that corresponds to the same case as the binary image in Figure 2.6 is shown in Figure 2.7.
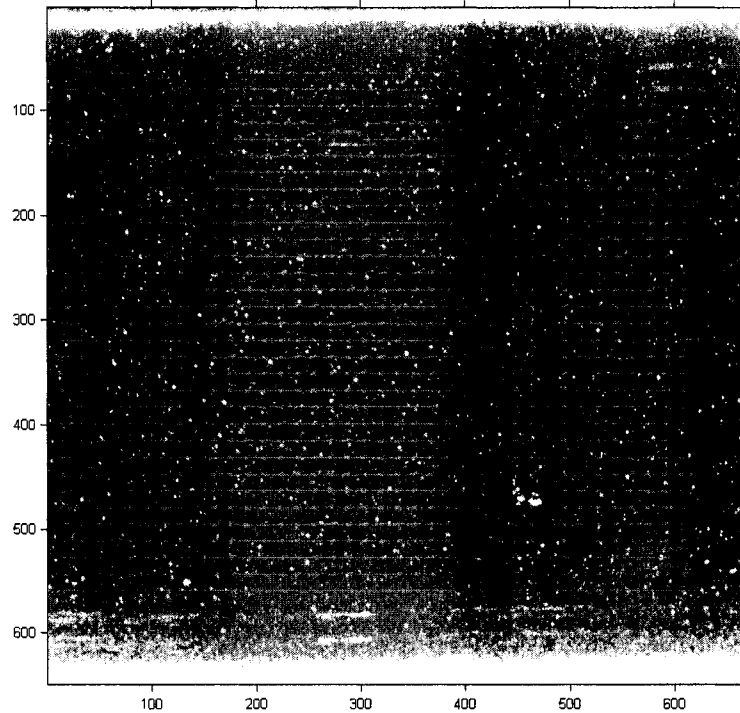
Figure 2.7: Sample velocity field.

2.2.2 PIV Setup

The PIV system used in the present study consists of a SoloPIV 120XT Nd:YAG laser and a CCD camera (JAI CV-M2) with the resolution of 1600 × 1200 pixels. The camera was connected to a PC equipped with a frame grabber (DVR Express, IO Industries, London, Ontario) that acquired 8-bit images at 30 Hz. For each experimental run, 1500 images (750 image pairs) were recorded. The timing of the laser pulses was controlled with a four channel digital delay

generator (555-4C, Berkely Nucleonics Corporation, San Rafael, CA). The time intervals between the two images of the image pair for all flow rates are presented in Table 2.1,

Table 2.1: Time Interval between the Two Images (Image Pair) for All Flow Rates

Mass Flow Rate [kg/s]	Pulse Interval [ms]
0.00781	2.5
0.00626	2.5
0.00494	3.0
0.00354	3.5
0.00232	4.0
0.00113	4.5

A beam from the laser was shone through the spherical and cylindrical lenses to form a laser sheet that was reflected up in the test section of the glass tube as shown in Figure 2.8. The laser sheet was located at the centre of the tube cross-section so that the long axis was parallel to the flow. The water was seeded with silver covered glass spheres (Potter Industries, Paoli, PA) with a mean diameter of 15 μm. With a specific gravity of 1.65, they were not neutrally buoyant. To check whether these particles were acceptable for these measurements, the particle response time was calculated using the following equation,

$$T_p = \frac{D_p^{\,2}}{36v_w}\left(1+2\frac{\rho_p}{\rho_w}\right)$$ (2.1)

where, T_p is the particle response time (Snyder and Lumley, 1971), D_p is the particle diameter, v_w is the kinematic viscosity of fluid, and ρ_p and ρ_w are

densities of particle and fluid, respectively (Siegel and Plueddemann, 1991). The response time is the time taken by the particles to respond to the changes in the flow. For the present study, the response time of particles was found to be 0.0268 ms. The smallest time scale of any flow is the Kolmogorov time scale. The Kolmogorov time scale for the present experiments ranged from 2.37 to 93.8 ms. The comparison shows that the response time of the particles is two to three orders of magnitude smaller than the Kolmogorov timescale of the given flow. Thus, it is concluded that the given tracer particles accurately follow the flow.
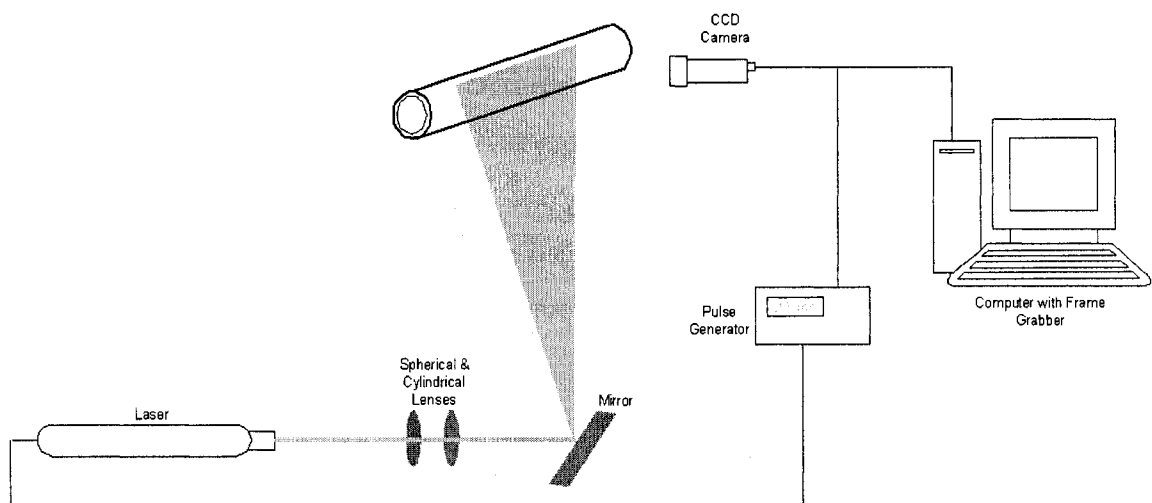

Figure 2.8: Schematic of the PIV setup.

2.3 Optical Effects Due to the Glass Tube

2.3.1 Glass Tube Assembly

Since the PIV technique requires optical access to the flow, the copper pipe at the test sections (the collector inlet and outlet) was replaced with the transparent glass tubes to act as a window. The glass tubes were connected to the copper pipe using ½ inch copper couplings. The couplings had an inner diameter of 16 mm, outer diameter of 17.5 mm, and a length of 25.9 mm. Figure 2.9 shows these components before they were assembled. After assembly, the glass window length was 25 mm.

To assemble the sections, the couplings were soldered to the copper tube first and then the glass tube was inserted into the coupling. Initially, glue was used to attach the glass to the coupling, but it was found that silicone provided a more flexible seal, so it was used for the remaining experiments. The flexibility of the seal was a welcome benefit because the glass was very brittle; any shock caused by moving the piece or tightening the fittings could have caused the glass to crack or break. The copper pieces near the glass tube were blackened to prevent unwanted reflections from the laser light as shown in Figure 2.10.
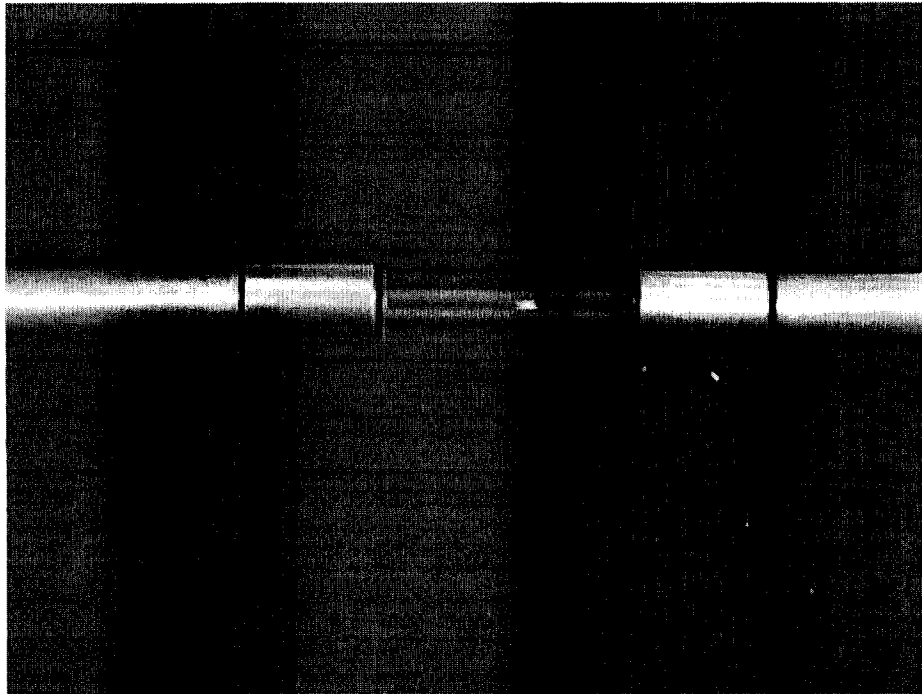
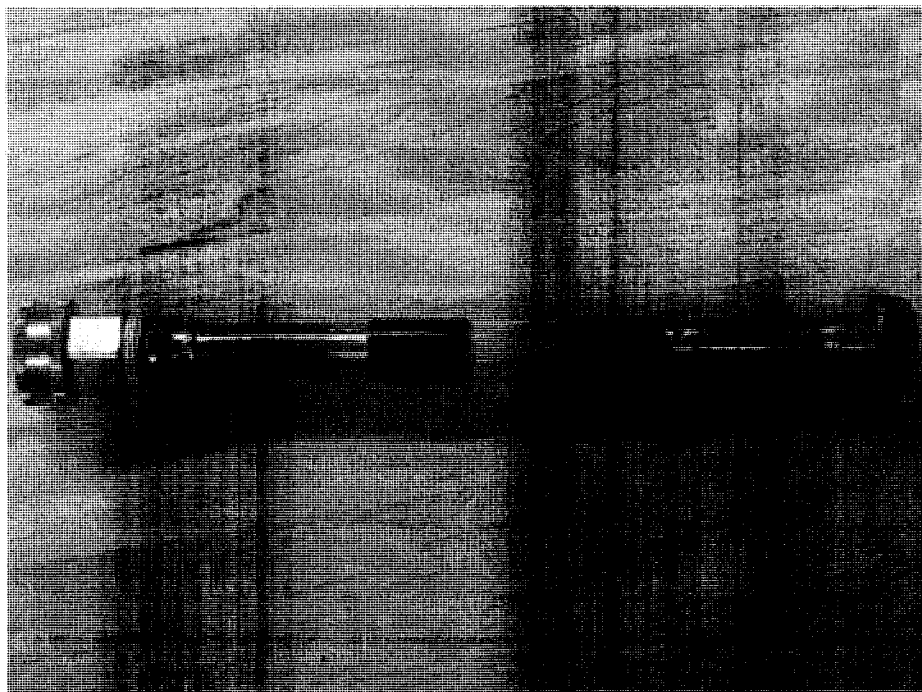Figure 2.9: Components of the glass tube assembly.

Figure 2.10: Inlet section piece, assembled.

2.3.2 Optical Effects Due to Water and Tube Curvature

An essential part of the PIV technique is the conversion of particle displacement from pixels in the image to real length units (cm). The conversion factor was determined by measuring the distance in pixels between graduations on an image of a ruler that was inserted into a water-filled tube. When analysing the image, the distances between graduations measured near the tube walls were much less than the distances measured at the centre of the tube. While developing a measurement scheme, two effects were noticed: distortion due the curvature of the tube and magnification by the water.

A couple of experiments were performed to examine these effects further by considering them separately. For these experiments, a set of special test strips of laminated strips of paper with solid dots printed on them (see Figure 2.11) and a ruler with vertical and horizontal graduations (see Figure 2.12) were prepared. Two test containers were developed, as well. One container had a flat glass wall and the other container was a glass tube (curved surface). The container with the flat glass wall was used to understand the magnification effect. An image of each test strip inserted into the water filled container was recorded. These images were compared with images of the strips in the container without water and without the container (only air). Specifically, the distance between the graduations on the ruler or corresponding edges of each dot was measured for all three media. It was noted that the degree of magnification depended on the distance between the strip and the glass or, the amount of water in front of the

strip. The distortion effect was examined by conducting a similar comparison with the other container. These experiments offered insight regarding how to determine the length scale. It was found that, even though the dots were solid circles drawn in AutoCAD, their edges could not be consistently selected resulting in inaccurate measurements. Therefore, it was decided to forego using them and only use the ruler. This decision was reinforced during the first collector experiment.
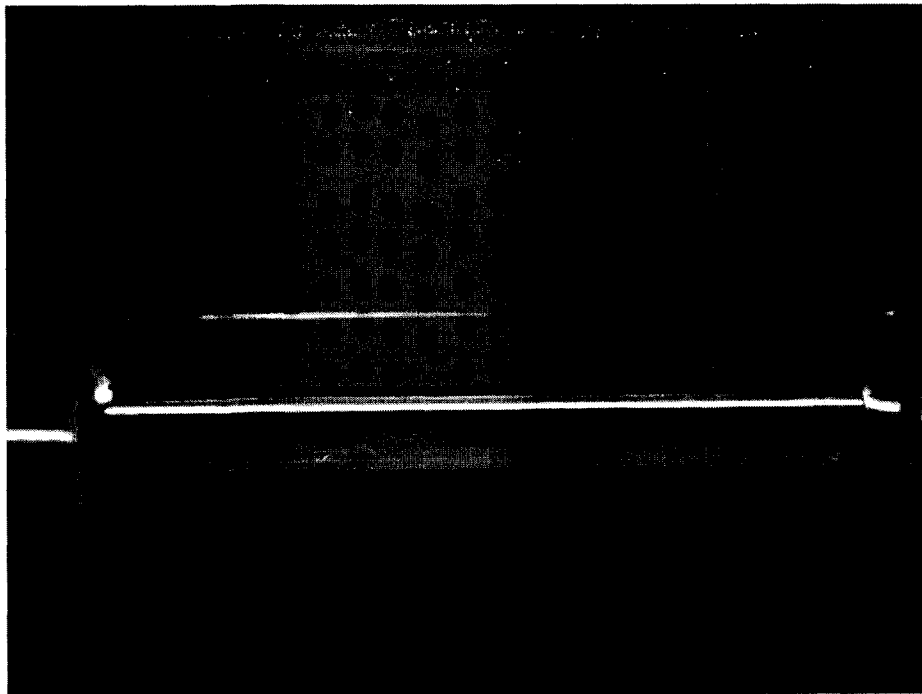
Figure 2.11: Image of the dotted-strip in the tube with water.
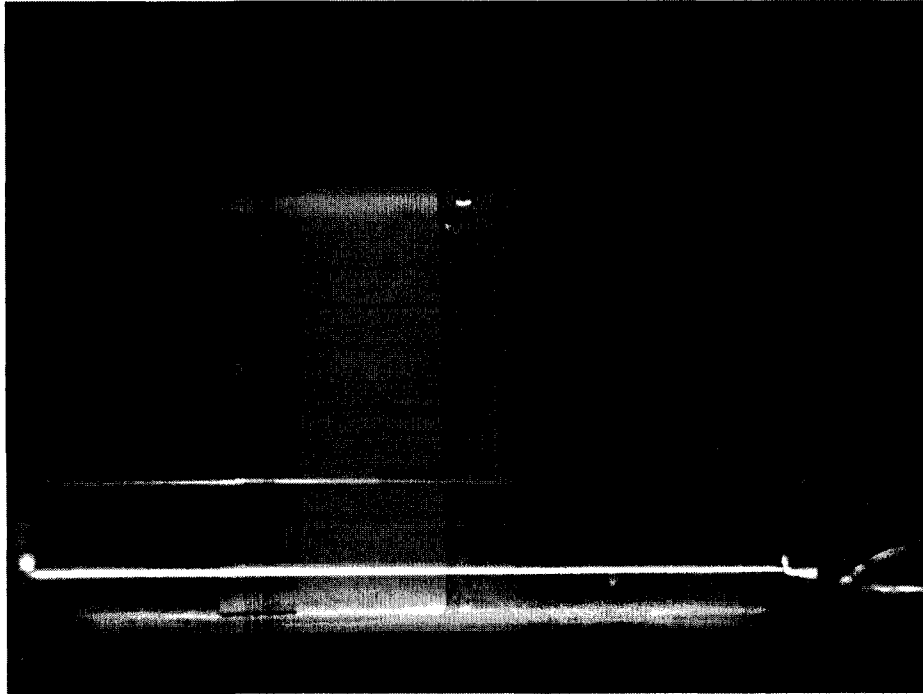
Figure 2.12: Image of the ruler-strip in the tube with water.

2.4 Length Scale Compensated for Optical Effects

2.4.1 Experiment Using Only the Tube

An experiment was conducted to verify that the PIV technique would yield positive results. They were conducted using a tube similar to Figure 2.10 at the inlet section of the apparatus. Problems arose when converting units. Since there was non-uniform vertical distortion, a parabolic correlation function was fitted to relate the displacement of the particles from pixels to cm using the following procedure. However, the resulting function was not accurate.

Using the ruler strip, the number of pixels between millimetre graduations in the image was measured. For each graduation line, its pixel location was determined by taking the average of five measurements along the line. The difference between successive graduations was tabulated to determine the calibration function. An additional check was performed to determine if the vertical location of the graduation line had any effect on the horizontal scale. It was checked by taking measurements at the same vertical location on the two longest graduations and comparing them.

All of the resulting measurements were consistent within acceptable error. The difference between the top and bottom of the vertical graduation lines was negligible which implies that the tube's curvature had no effect on the horizontal scale. The horizontal conversion factor was considered to be constant. The vertical scale, however, was affected by the curvature of the tube. The measured number of pixels per millimetre was plotted against the vertical location and a second order best-fit line was fitted to the data.

There are a few sources of error for the measurements. For one, it had to be determined what constitutes the edge of the graduation line. Every effort was made to be consistent. As well, anything that could have caused the ruler to not be perfectly parallel or perpendicular to the flow, such as a slight tilt in the strip, may have had an effect. Again, these were minimised as best as possible.

While the resulting function for the vertical scale was second order, a symmetric parabola could not be fitted because there was not enough data and too much variation. With very little confidence in these results, a modification to the apparatus was made: a water-filled box surrounding the glass tube was assembled to eliminate the effects of the curvature.

2.4.2 Experiments Using a Water-Filled Box

The distortion effects were removed by using a water-filled box surrounding the glass test tube. Consider that light rays from the particles in the flow must bend twice. First, they bend because of the interface between the water and the inside wall of the glass. Then they bend at the interface between the outside wall of the glass and the outside fluid. From the law of diffraction, the angles of incidence and refraction are related by the index of refraction of the two materials:

$$n_1 \sin i = n_2 \sin p \qquad (2.2)$$

where n_1 and n_2 are the indices of refraction of the two materials, respectively; i is the angle of incidence; and r is the angle of refraction. As shown in Figure 2.13, when air is the surrounding fluid, the light will not bend enough and the images will appear distorted. When the surrounding fluid is water, the distortion effects are negated because the indices of refraction are the same; the image appears magnified. The magnification effects affect all particles equally so that when acquiring the image of a ruler inserted inside the tube at the measurement

54

location, the graduations on the ruler are also magnified by the same factor. Therefore, having a water-filled box ensures that the measured vertical displacement of the particles was constant.
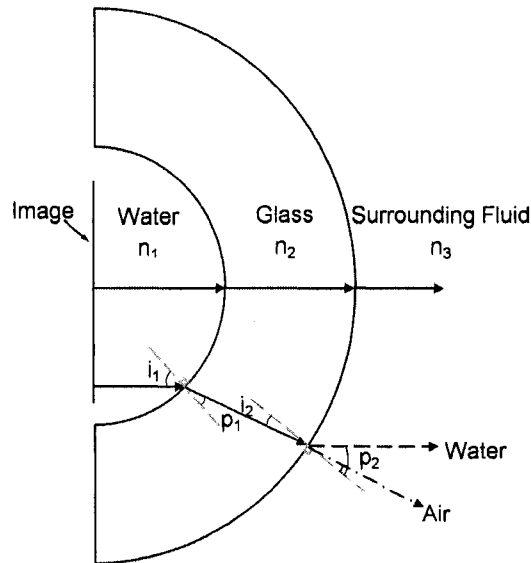
Figure 2.13: Refraction due to the changing materials.

2.4.3 The Surrounding Box

The surrounding box was made of 3 mm thick acrylic on three sides. The bottom and front walls are made of glass to allow good optical access to the camera (through the front wall) and laser light sheet (through the bottom wall). The glass sections were made from Pyrex glass. The dimensions of the front and bottom section are 60 mm × 47 mm and 44 mm × 60 mm, respectively. The side walls were 44 mm × 44 mm with a 20 mm hole on two side walls for the coupling. The centre of the hole was located 20 mm from the bottom (see Figure 2.14). Installation of the surrounding box at the collector inlet was straightforward. One

of the fittings was removed so that the box could slide on and be set in place using silicone. The fitting was then replaced (see Figure 2.14).
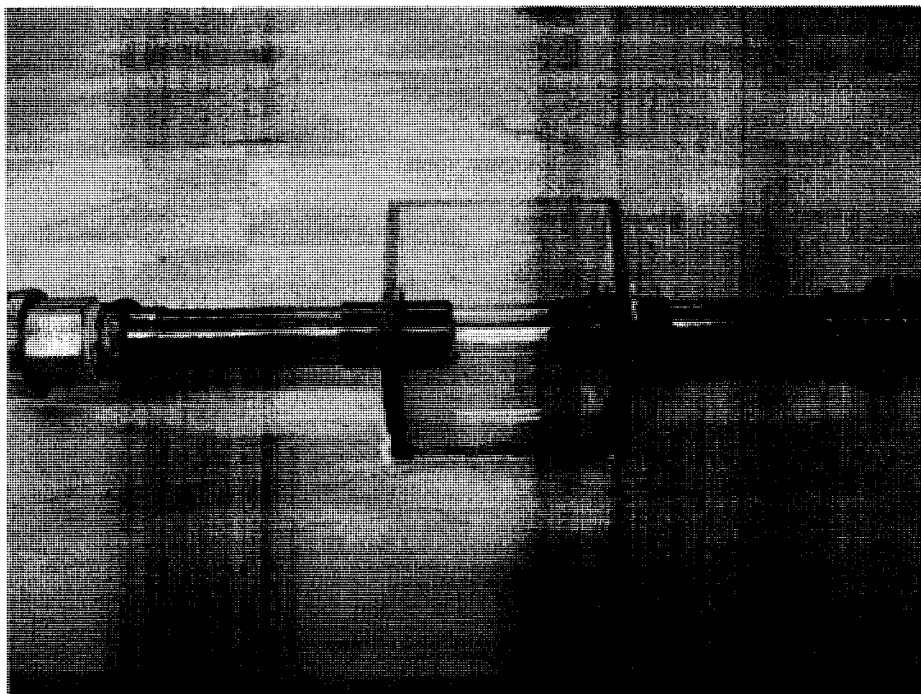
Figure 2.14: The surrounding box at the inlet.

The installation of the surrounding box and the glass window at the collector outlet required more work. The tube was cut and a coupling was installed immediately next to the edge of the plate. A second coupling was affixed to the removed tube. Before the two pieces were rejoined, the box was slid onto the tube. The glass tube was affixed to the other coupling and the box attached in the proper place as shown in Figure 2.15. Wooden stands, one at the inlet and one under the collector, were built to support the apparatus and reduce the load on the glass tube.
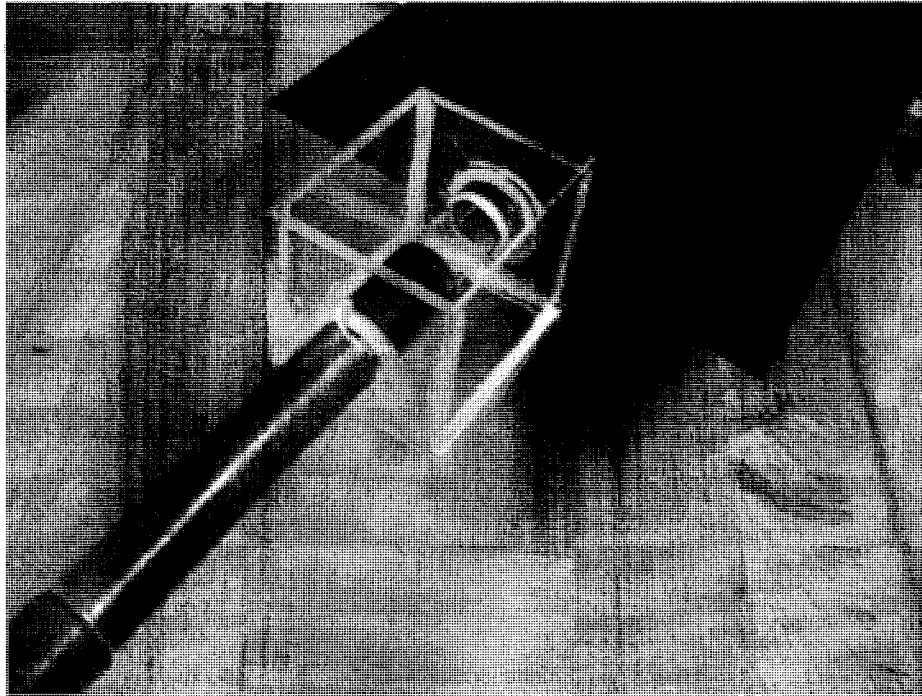
Figure 2.15: The surrounding box at outlet.

Using the same measurement procedure, the conversion factors between pixels and cm were computed. The variation amongst all of the individual data points was on average, within 4 pixels, which shows that using a constant factor was acceptable. The sources of error in the measurements are the same as before.

2.5 Experimental Procedure

Before each experimental run, water at a high flow rate was pumped through the system for 10 minutes to remove any air bubbles that may have been trapped inside. For the heated experiments, the heater was also turned on and set to the surface temperature (300°C or 400°C), and left to reach steady state. Placed 50 mm above the collector, the heater surface temperatures produced absorber

surface temperatures that are similar to what would be achieved under operating conditions with the sun. Experiments were also conducted for an unheated condition.

The experimental procedure was as follows:

- Adjust the flow rate.

- Set the pulse generator to the correct time interval.

- Wait 10 minutes for the flow and temperature to reach steady state.

- Check and clean the exterior of the glass tube to remove any bubbles.

- Turn on the laser and begin recording the temperature measurements using LabVIEW.

- Record the PIV images.

- Turn off the laser and stop recording temperature data.

- Process one image pair and check its velocity field to ensure that the data is satisfactory.

- Repeat the procedure for each flow rate.

At the end of a set of experiments, the heater was turned off, but the pump was kept on for a few minutes for the system to cool. The interior of the glass tube was cleaned with a soft brush to remove any particles that had accumulated along the wall during the experiments.

2.6 Uncertainty Analysis

2.6.1 Error Estimate for the PIV Measurements

As outlined in Cowen and Monismith (1997) the total error in PIV measurements is the sum of errors due to gradients, particle diameter, out-of-plane motion, dynamic range, peak locking and AGW interpolation. The procedure used to estimate the error was adapted from Siddiqui (2002). The non-dimensional particle diameter in the present study was 0.67 pixels. Particles that are smaller than one pixel always occupy on pixel area in a PIV image. Consequently, the true position of the particle within a pixel cannot be resolved.

According to Fincham and Spedding (1997), peak locking occurs in any type of image velocimetry technique where sub-pixel determination of the correlation peak is attempted. However, it can be minimized by using a suitable peak-fitting scheme. There are several sub-pixel peak fitting schemes that include the three-point Gaussian, parabolic and centre-of-mass estimators. The three-point Gaussian estimator was considered to be the best sub-pixel fit (Cowen and Monismith, 1997).

The results of Cowen and Monismith (1997) and Prasad et al. (1992) were used to estimate the errors in the PIV data. The errors were estimated using the raw data. A detailed procedure to estimate the errors in the PIV data is given below.

1. The mean values of the largest velocity gradients in the streamwise and vertical directions were computed from the raw PIV data. In the present study, the mean streamwise velocity gradients were 1% and the mean vertical velocity gradients were zero. Thus, the mean streamwise velocity gradients were considered for the error estimation.

2. The error due to velocity gradients were estimated using Figure 5(e) in Cowen and Monismith (1997). This figure gives the approximate errors due to velocity gradients and is based on a particle size of 2.0 pixels. The total error due to velocity gradients is the sum of the mean and RMS errors. The error due to velocity gradient was estimated to be:

$$\varepsilon_u = 0.08 \text{ pixels (based on 1\% gradient)} \qquad (2.3)$$

where ε_u is the errors associated with the streamwise velocity.

3. Since the particle diameter in the present study was 0.67 pixels, the errors due to smaller particle diameter should be accounted for. Figure 5(a) in Cowen and Monismith (1997) was used, which is the plot of the errors as a function of the particle size. The errors due to a particle diameter of 1.0 pixel were estimated since this was the smallest particle diameter that Cowen and Monismith (1997) considered. The error for a particle diameter of 1.0 pixel and the same velocity gradients was:

$$\varepsilon_u = 0.07 \ pixels \qquad\qquad (2.4)$$

4. The errors corresponding to a particle diameter of 0.67 pixels were estimated using Figure 13 in Prasad et al. (1992), which shows the variation in the bias (peak locking error) and RMS errors as a function of particle diameter. Using the figure, the estimated errors associated with a particle diameter of 0.67 pixels would be 20% larger than the errors associated with a particle diameter of 1.0 pixel. The estimates of Prasad et al. (1992) were based on center of mass peak-fitting scheme, which is the scheme that is most susceptible to peak-locking errors (Fincham and Spedding, 1997). The errors in the present case would be smaller because a three-point Gaussian estimator, which is much less susceptible to peak locking than the center of mass scheme (Cowen and Monismith, 1997), was used. Therefore, a more realistic estimate of the increase in the errors is 10% due to the small particle size. Hence, the final error estimate based on 10% increase in errors was:

$$\varepsilon_u = 0.157 \ pixels \qquad\qquad (2.5)$$

5. The in-plane vertical displacement based on the mean and standard deviation of the vertical displacement was estimated to be:

$$W = \overline{w} + \sigma_w = 0.5955 \, pixels \approx 13.3 \mu m \qquad\qquad (2.6)$$

The out-of-plane motion was expected to be less than or equal to the vertical displacement. Since the thickness of the laser light sheet was approximately 200 μm, the out-of-plane motion in the present case was assumed to be negligible.

6.   The error due to AGW interpolation was estimated from Figure 5(f) in Cowen and Monismith (1997) and it was 0.058 pixels. Thus, the total error in the streamwise velocity was estimated to be:

$$\varepsilon_u = 0.077 + 0.08 = 0.157 \text{ pixels} \tag{2.7}$$

This RMS error expressed in velocity units is:

$$\varepsilon_u = 0.175 \text{ cm/s} \tag{2.8}$$

It was assumed that the errors in the vertical velocity (w) were the same as the errors in the streamwise velocity (u). Since the larger gradients in the vertical direction (ie: $\partial u/\partial z$) will produce errors in both u and w, the error in V, where $V = \sqrt{u^2 + w^2}$ is:

$$\varepsilon_u = 0.248 \text{ cm/s} \tag{2.9}$$

The errors in the vorticity measurements were estimated from the errors in the velocity measurement. The vorticity (ω) is given by:

$$\varpi = \frac{\partial u}{\partial z} - \frac{\partial w}{\partial x} \qquad (2.10)$$

where $\partial u / \partial z$ and $\partial w / \partial x$ are the streamwise and vertical velocity gradients, respectively. The streamwise velocity gradient can be written as:

$$\frac{\partial u}{\partial z} = \frac{\Delta w}{\Delta x} \qquad (2.11)$$

where $\Delta u = u_1 - u_2$, that is, the difference in the streamwise velocities at two grid points and Δz is the vertical distance between two grid points. The central difference method was used to compute vorticity; therefore, Δz in the present case is equal to 0.071 cm (32 pixels × 0.002234 cm/pixel). The variance of the errors (ε^2) in Δu can be estimated as:

$$\varepsilon^2(\Delta u) = \varepsilon^2(u_1) + \varepsilon^2(u_2) = 2\varepsilon^2(u) = 2(0.175)^2 = 0.0612 cm^2 s^{-2} \qquad (2.12)$$

where $\varepsilon^2(\Delta u)$, $\varepsilon^2(\Delta u_1)$ and $\varepsilon^2(\Delta u_2)$ are the variance of the errors in Δu, u_1, and u_2, respectively (Kennedy and Neville, 1976). The variance of the errors in $\partial u / \partial z$ is then given by:

$$\varepsilon^2(\Delta u / \Delta z) = \varepsilon^2(\Delta u) / \Delta z = 0.0612/.071 = 0.862 s^{-2} \qquad (2.13)$$

Since the assumed magnitude of the errors in w was equal to those in u, the variance of the errors in $\partial w / \partial x$ is given by:

63

$$\varepsilon^2\left(\Delta w/\Delta x\right) = \varepsilon^2\left(\Delta w\right)/\Delta x = 0.0612/.071 = 0.862 s^{-2} \qquad (2.14)$$

where Δx is equal to 0.071 cm (32 pixels × 0.002234 cm/pixel). The variance of the errors in the vorticity, $\varepsilon^2(\Delta\omega)$, is then given by:

$$\varepsilon^2\left(\varpi\right) = \varepsilon^2\left(\Delta u/\Delta z\right) + \varepsilon^2\left(\Delta w/\Delta z\right) = 1.727 s^{-2} \qquad (2.15)$$

Thus, the RMS error in the vorticity, $\varepsilon^2(\Delta\omega)$, is then given by:

$$\varepsilon\left(\varpi\right) = \sqrt{\varepsilon^2\left(\varpi\right)} = 1.31 s^{-1} \qquad (2.16)$$

Hence, the average RMS errors in the instantaneous velocity and vorticity estimates are ±0.24cm/s and ±1.31s^{-1}.

Chapter 3 – Results and Analysis

3.1 Data Reduction

The average temperatures of the water and pipe surfaces for each experiment were obtained by time averaging. The water properties were calculated at the average water temperature ($T_{f,avg}$) computed as:

$$T_{f,avg} = \frac{T_{f,o} + T_{f,i}}{2} \qquad (3.1)$$

Following Barozzi et al. (1985), the average heat transfer rate per unit length to the water was calculated by considering the overall enthalpy rise of the water as:

$$q_l = \frac{\dot{m}C_p\left(T_{f,out} - T_{f,in}\right)}{L} \qquad (3.2)$$

The average wall heat flux was computed by:

$$q_w = \frac{q_l}{\pi D} \qquad (3.3)$$

To account for the variation in the inlet water temperature for each experiment, the temperature data was normalized by the inlet fluid temperature as done by Habib and Negm (2001):

$$\theta = \frac{T - T_{f,in}}{q_i / \pi k_f}$$
(3.4)

where, θ is the normalized temperature, and k_f is the thermal conductivity of water (Habib and Negm, 2001). The average Nusselt number was calculated as (Mohammed and Salman, 2007):

$$Nu_m = \frac{q_w D}{(T_w - T_{f,b})k_f}$$
(3.5)

The average Grashof number is calculated using the following relation:

$$Gr = \frac{g\beta D^3 (T_w - T_{f,b})}{v^2}$$
(3.6)

The dimensionless parameters that are relevant for mixed convection heat transfer in pipes are:

Reynolds Number
$$\mathrm{Re} = \frac{uD}{v}$$
(3.7)

Prandtl Number
$$\mathrm{Pr} = \frac{v}{\alpha}$$
(3.8)

Rayleigh Number
$$Ra = Gr\mathrm{Pr}$$
(3.9)

Richardson Number
$$Ri = \frac{g\beta D(\overline{T_w} - \overline{T_{f,b}})}{u^2}$$
(3.10)

As described in Chapter 2, experiments were conducted at two heating conditions that correspond to the heater temperatures of 300°C and 400°C and with the collector unheated. For each condition, the experiments were conducted at six flow rates. Since the density and viscosity change when heat is applied, the volumetric flow rate and Reynolds number vary at each flow rate for the heated and unheated conditions. Therefore, the results are presented in terms of mass flow rate. The mass flow rates considered were: 0.00781 kg/s, 0.00626 kg/s, 0.00494 kg/s, 0.00354 kg/s 0.00232 kg/s and 0.00113 kg/s. Hereinafter, they will be referred to as Case I to VI, respectively. However, there is no data for Case VI at 400°C because water in the tube began to evaporate under those conditions.

3.2 Temperature Results

The water temperature at the inlet and outlet of the collector were recorded during each experiment. The temperature of the collector tube surface was also recorded at three circumferential locations: top, bottom and the plate-tube joint. These measurements were made at three axial locations of the tube: the inlet, the middle and the outlet. The temperatures used for the analysis are the time-averaged values at each location.

When heat was applied, the temperature of the water increased as it passed through the collector, as expected. Figure 3.1a shows the increase in water

temperature inside the collector for all heated cases. The plot shows that the change in water temperature between the inlet and outlet decreased with an increase in the flow rate. The same trend is shown when examining the normalized temperature increase (Figure 3.1b). It is clear that there is an exponential relationship between the change in water temperature and the Reynolds number.
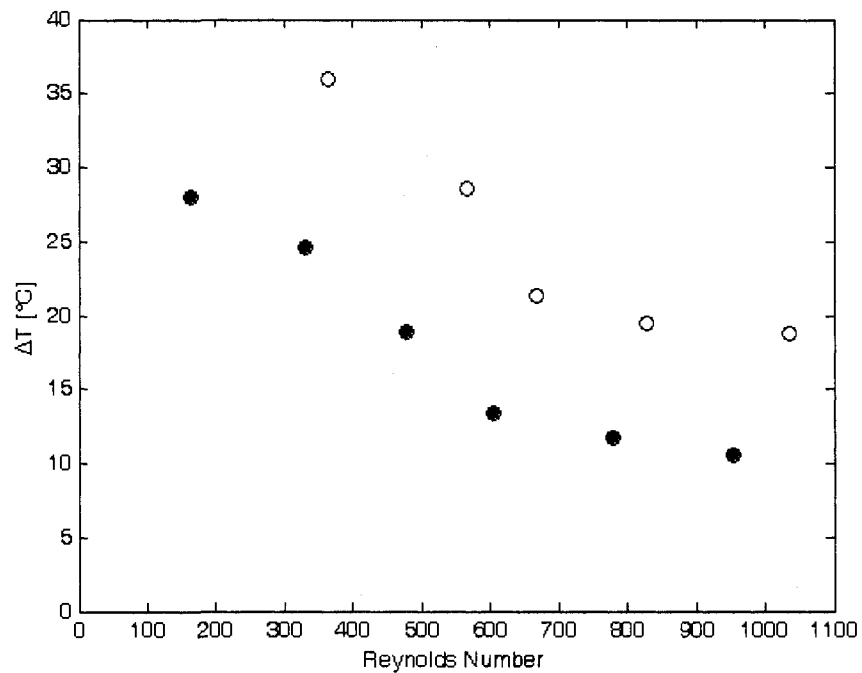

Figure 3.1a: Change in water temperature for the heater temperatures of 300°C (●) 400°C (○).
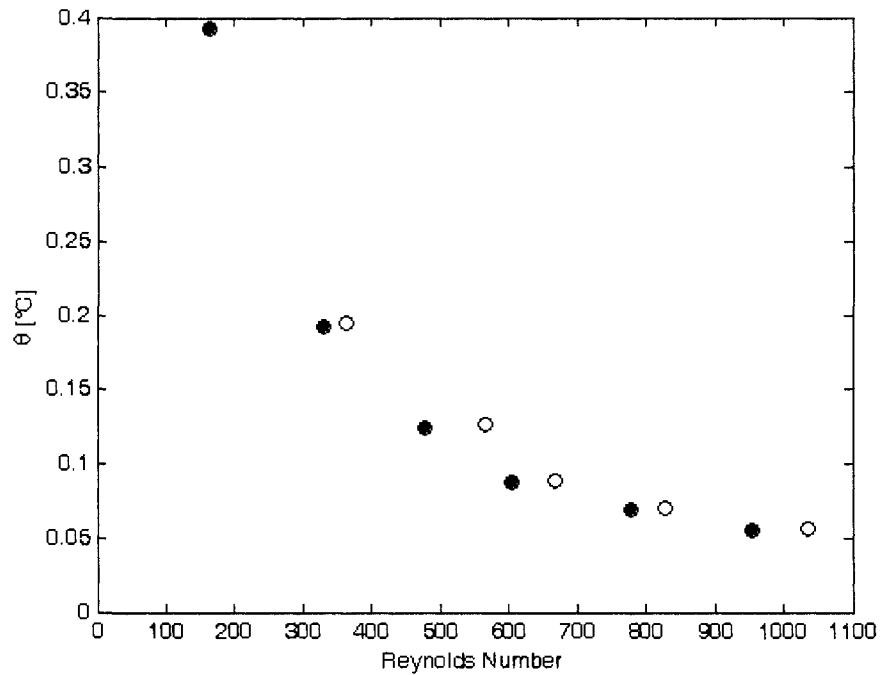
Figure 3.1b: Normalized change in water temperature for the heater
temperatures of 300°C (●) 400°C (○).

The circumferential wall temperatures at the inlet (Figure 3.2a), middle (Figure 3.2b) and outlet (Figure 3.2c) of the collector tube are plotted for both heater surface temperatures (400°C and 300°C). The trends are similar for both heating cases. To understand the phenomenon, the heat exchange between within the tube wall, within the water, and between the tube and the water must be considered.

Comparison of Figures 3.2a to 3.2c shows that along the circumference, the wall temperatures at the inlet and exit are lower than that in the middle of the collector. This is likely due to the axial conduction heat loss upstream and downstream from the inlet and exit, respectively.
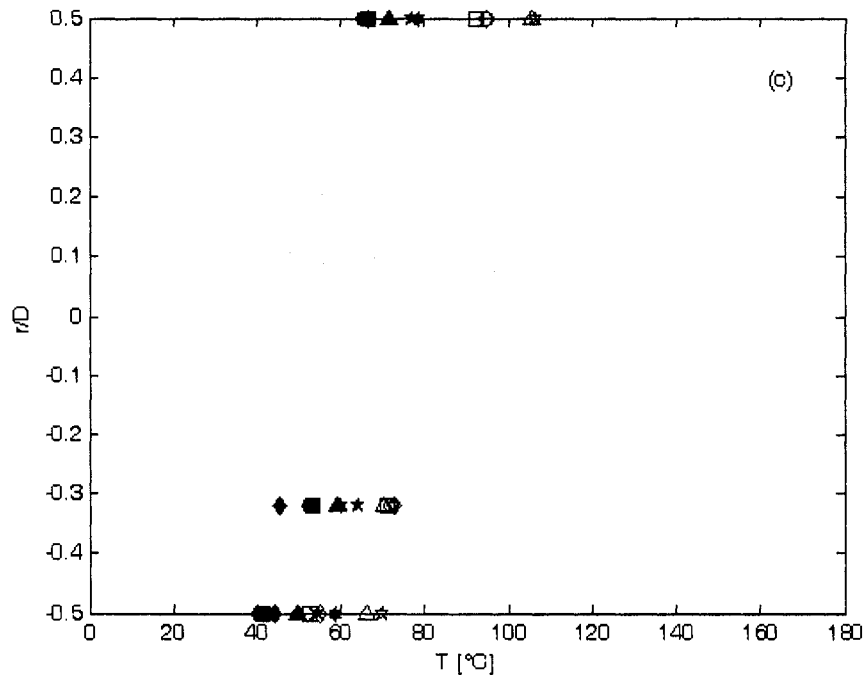
69
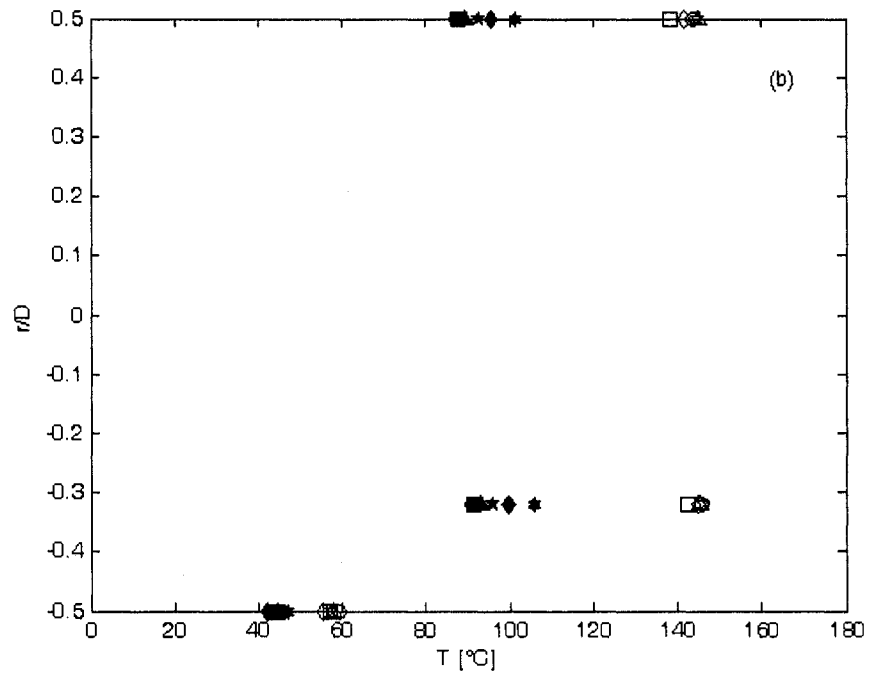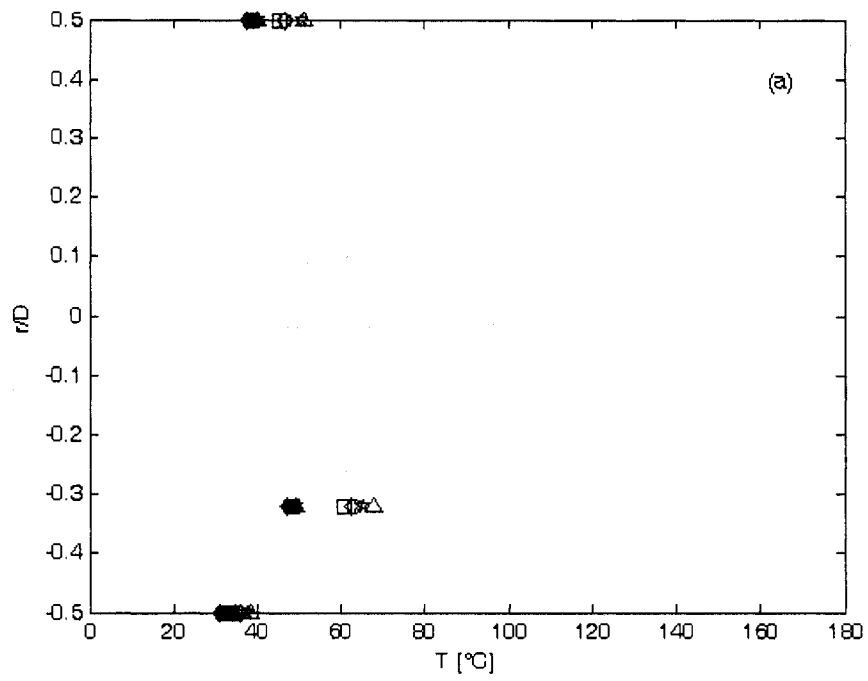
Figure 3.2: Circumferential wall temperature at each flow rate at heater temperatures of 300°C (Closed Symbols) and 400°C (Open Symbols) at (a) inlet, (b) middle, (c) outlet.
Case I (●), Case II (■), Case III (♦), Case IV (▲), Case V (★), Case VI (✱)

Figure 3.2a shows that the collector wall temperature increases from the top of the tube until the joint of the collector tube and plate, which is located in the lower half of the tube (see Figure 2.2 and 2.3 in Chapter 2). The maximum temperature is observed at this location at all flow rates for both heater temperature cases. The wall temperature decreased until it reached the bottom of the tube where the lowest temperature was observed. For the 300°C experiments, the wall temperature at the joint was 20.1% higher than that at the top of the tube and 30.7% higher than the temperature of the bottom of the tube at the highest flow rate (Case I). These percentages changes to 18.5% and 34.5%, respectively, at the lowest flow rate (Case VI). The temperature difference between the top and

71

bottom of the tube was 15.3% and 24.4% at highest and lowest flow rates, respectively. As the flow rate changed, there was no clear trend as to its affect on the wall temperatures. This is probably due to axial conduction in the tube wall upstream. The differences between the highest and lowest temperatures were 8.1% at the top, 5.59% at the joint, and 12.6% at the bottom. At the heater surface temperature of 400°C, the temperatures at the top and bottom were 26.1% and 43.2% higher than that at the joint for the highest flow rate (Case I), respectively. At the lower flow rate (Case V), the differences decrease to 22.3% and 42.2%, respectively. The temperature at the top was 30.0% higher than the bottom for the highest flow rate, and 34.4% higher for the lowest flow rate. As the flow rate changed, there was a 13.3% difference between the highest temperature and lowest temperature recorded at the top of the tube; 11.4% at the joint; and 10.6% at the bottom. For each flow rate, raising the heater temperature from 300°C to 400°C resulted in an increase in the measured wall temperatures. At the inlet, the temperature increases due to the heater temperature increase ranged from 16.1% to 27.7% at the top, 25.8% to 37.8% at the joint, and 3.37% to 16.5% at the bottom.

This distribution can be explained by a considering the heat transfer process at this section. The heat influx to the upper portion of the tube is through thermal radiation which is conducted circumferentially around the tube wall. Whereas, the radiant heat incident on the plate is conducted through the joint to the tube. Due to the larger surface area of the plate compared to the tube, the radiant heat

72

flux incident on the plate is higher than the tube. Thus, the heat transfer at the joint is higher than the circumferential heat transfer, which results in higher wall temperature at the joint. The heat transfer to the portion of the tube above the joint is due to radiation and circumferential conduction heat transfer. The heat transfer to the portion of the tube underneath the joint is only due to circumferential heat transfer as this section is not exposed directly to the incident thermal radiation. There is also heat conduction along the tube axially. The axial conduction upstream preheats the fluid inducing secondary flow due to natural convection.

As the water is heated from the bottom, it rises and is replaced by water from the upper portion inducing unstable stratification due to continuity. However, near the upper edge of the tube, the warm and less dense water remains in the upper portion inducing stable stratification. Ouzzane and Galanis (2001) numerically analyzed a tube with an external longitudinal fin and noted that the circumferential distribution of the interfacial heat flux peaked in the area near the plate which is consistent with the present experimental observation. They also showed that, except for a short distance at the tube's entrance, the energy to the water is split unevenly with most coming from the bottom half of the tube. This occurs because the warmer fluid accumulates in the top part of the tube cross-section due to buoyancy.

The circumferential tube wall temperature distribution at the middle of the tube is shown in Figure 3.2b. The plot shows that the temperature at the top is very close to the temperature at the joint at the middle of the tube. The heat transfer analysis presented above suggests that the temperature at the joint should be higher than that at the top of the tube. For Case I, the temperature at joint of the tube is 4.09% higher than that at the top and 51.8% higher than the bottom at the lower heater temperature. The temperature at the top was higher by 98.9% compared to the bottom of the collector tube. For Case VI, the temperature at the joint was higher by 4.14% than the top and 55.6% higher than the bottom. The temperature at the top was 115.7% higher than the bottom. Generally, the wall temperatures increased with flow rate. As the flow rate changed, the difference between the largest and smallest temperatures measured was 16.3% at the top, 16.4% at the joint and 11.3% at the bottom. At the heater temperature of 400°C, the wall temperature at the joint was 1.64% and 59.4% higher than at the top and bottom, respectively, for Case I. For Case V, the temperature at the joint was 0.97% and 60.8% higher than the top and bottom, respectively. The temperature at the top was 142.3% higher than the bottom at the highest flow rate and 152.8% higher at the lowest flow rate. At this heater temperature, the results did not indicate a trend with respect to flow rate. The difference between the maximum and minimum recorded wall temperatures for the five cases were 5.07%, 2.82%, and 7.21% for top, joint, and bottom of the collector tube, respectively. The wall temperatures were higher when the heater surface was at 400°C. The increase ranged from 48% to 64.5% at the top of the tube, 44.9% to

74

60.5% at the joint, and 25% to 35.1% at the bottom. The higher top wall temperature suggests that the heat transfer to water in the upper portion of the tube is reduced. This is due to the formation of stably stratified layer in the upper portion of the tube which results in less fluid mixing and hence reduced heat transfer. The numerical results of Ouzzane and Galanis (2001) showed that the top half of the tube eventually behaves almost isothermally. However, the significantly large temperature gradients between the water and tube wall observed in the present study suggests that it is very unlikely to have a fluid layer in the upper half of the tube. Detailed water temperature measurements inside the tube are necessary to understand the actual thermal structure.

The circumferential wall temperature distribution at the outlet is shown in Figure 3.2c. The results show that the temperature is highest at the top of the tube and decreased gradually toward the bottom for the 300°C experiments. The temperature was 19.9% higher at the top than at the joint and 61.6% higher than the temperature at the bottom for Case I. For Case VI, these differences changed to 23.8%, 1.63% and 33.4%, respectively. The general trend was that the wall temperature increased with flow rate. Subsequently, the differences between the maximum and minimum temperatures (due to flow rate variation) were 19.9%, 41.4%, and 45.3% at the top, joint and outlet, respectively. At the higher heater temperature, the wall temperature at the top was higher than the temperature at the joint by 24.2% for Case I and 31.6% for Case V. Compared to the temperature at the bottom of the collector tube, the temperature at the top

was 83.2% and 52.4% for the highest and lowest flow rates, respectively. The joint temperature was 27.9% higher than the bottom for the highest flow rate and 3.98% higher for the lowest flow rate. At the bottom, the wall temperature increased with flow rate. However at the other two locations, the relationship was not clear. The difference between the largest and smallest wall temperatures recorded were 15.2%, 3.17% and 34.7% at the top, joint and bottom, respectively. As the heater surface temperature was increased to 400°C, the increases in measured wall temperature ranged from 38.2% to 47.3% at the top, from 13.5% to 60.8% at the joint and from 25.3% to 33.9% at the bottom.

This shows that the stable fluid layer at the top causes an additional resistance to the heat transfer to the bulk fluid throughout the collector. These results also indicate that the heat transfer to the fluid is heavily weighted towards the bottom, and also suggests that the water inside the tube is divided into two distinct zones comprised of stable and unstable layers. The interaction between the two layers and the superposition of the buoyancy-driven convective motions on the mean axial flow make the flow field complex.

Figure 3.3 shows that the average wall heat flux increases as the flow rate increases for both heater surface temperatures. Since the heater surface temperature was constant, this result implies that there is more radiant exchange between the collector and the heater surface at the higher flow rates. These observations are consistent with Hobbi (2007).
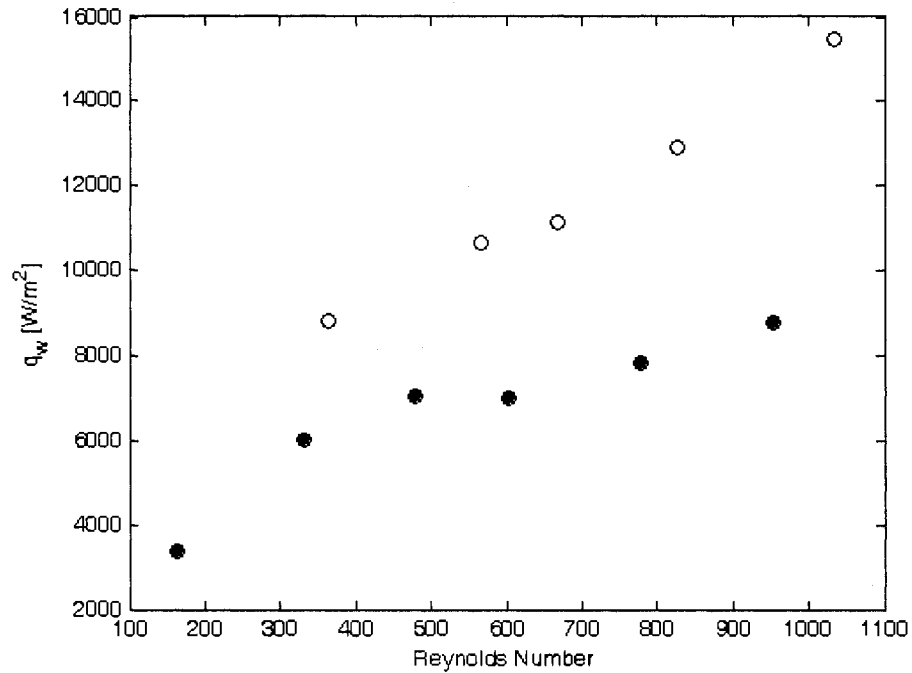
Figure 3.3: Average wall heat fluxes for heater temperatures of
300°C (•) 400°C (o).

3.3 Mean Velocity

The mean velocity was computed by averaging the velocity data at each depth

temporally and spatially. That is, the time series were extracted at each grid point

for each experimental run. The average velocity was obtained at each grid point

by time-averaging. The time-averaged velocities at all grid points at a particular

radial location were then spatially averaged. This provided the spatial-temporal

averaged velocity at each radial location. Due to particle accumulation on the top

and bottom walls of the tube, the data in those areas was rendered inadequate.

Using a threshold image, as described in Section 2.2.1, these and other problem

areas on the images (due to bubbles, reflections, etc.) were not considered in the

analysis. Due to the unavailability of reliable data in these regions, some of the resulting profiles are incomplete near the tube walls.

As mentioned in Chapter 2, the velocity fields inside the collector were measured at the two heated conditions (300°C and 400°C heater surface temperatures) and an unheated condition. This allows an investigation in the impact of radiant heating (solar heating in the actual case) on the flow behaviour inside the collector tube.

3.3.1 Unheated Collector

The experiments without any applied heat were performed for two orientations of the apparatus. For the unheated condition, the velocity fields were measured at a section immediately upstream of the collector. Since the flow is developed, the velocity profile at this section is expected to be unchanged through and downstream of the collector. For the first orientation, the collector tube was setup in a way that the flow direction was from west to east. While for the second orientation, the collector was rotated by 90° and the flow direction was from north to south. The mean velocity profiles at the two collector orientations for all flow rates are plotted in Figures 3.4a to 3.4f for cases I to VI, respectively. The analytical velocity profile for the laminar flow in a tube or channel has a parabolic shape with the maximum velocity along the centreline of the tube (Fox, 2004). The results, however, showed that the velocity profiles behave differently with the

change in the orientation of the tube. It is observed that when the flow direction is towards the east, the maximum velocity is shifted towards the upper half of the tube resulting in an asymmetric mean velocity profile across the tube. As the tube orientation is changed to south, the maximum velocity location moved closer to, but still above, the tube centreline. Also, the peak location moved towards the centreline as the flow rate decreased.

The asymmetry in the profile may be caused by the Coriolis force due to the Earth's rotation. Draad and Nieuwstadt (1998) investigated the effect of Coriolis forces on the laminar flow in pipes. Through experimental and numerical analyses, they concluded that the Coriolis Effect is significant for laminar flow in the high Reynolds number range. Using Laser Doppler Velocimetry, they observed velocity profiles that had deviated significantly from the theoretical parabolic shape despite taking precautions to eliminate all sources of flow disturbances. Through perturbation analysis of the continuity and Navier-Stokes equations, they showed that the Coriolis forces have an effect in the r– and θ– directions that must be balanced by a viscous force. As a result, there is secondary flow in the radial direction which, by balancing inertial and viscous forces, influences the axial velocity. The Ekman number, Ek, relates the viscous force to the Coriolis force and is given as:

$$Ek = \frac{\nu}{2\Omega D^2 \sin \alpha}$$ (3.11)

where, v is the kinematic viscosity, Ω is the angular velocity of the Earth, D is the pipe diameter, and α is the angle between the pipe axis and the Earth's rotation axis (Draad and Nieuwstadt, 1998). Using the results of linear perturbation analysis that was conducted by Benton (1956), they concluded that the secondary flow is very weak but significantly modifies the velocity profile for their cases (Ek = 5.23 at high Reynolds number). They also showed that the Coriolis effects scale with the Reynolds number. After solving the Navier-Stokes equations numerically, they observed axial velocity profiles in the horizontal and vertical planes that deviated from the theoretical shape, too. It is important to remember that their experiments were for long pipes with a large diameter. They suggested that the reason that this phenomenon has not been previously seen for smaller diameter pipes using water as the fluid is because the Ekman number increases as the pipe diameter decreases which means that the Coriolis effects become less significant.

Based on the approximate values of α for the present experiments, the Ekman number was estimated to be 26.3 and 37.2 for east-bounded and south-bounded flow cases, respectively. This indicates that the Coriolis forces have relatively larger influence on east-bounded flow compared to the south-bounded flow. This is also evident from the mean velocity profiles in Figure 3.4 which shows that the deviation of the peak velocity from the pipe centerline is more significant for east-bounded flow compared to the south-bounded flow.

The present results show that this phenomenon is also very significant in small diameter pipes where the Ekman number is relatively large. In addition to the Draad and Nieuwstadt (1998), an asymmetric velocity profile has been observed in a square channel at low Reynolds laminar flow by Gajusingh (2006). More experiments at several different tube orientations and geometry need to be done to further explore this phenomenon.

Although the solar collectors are installed south facing, the present results suggests that the orientation of collector tubes with respect to the flow direction would influence the flow behaviour inside the collector tube and could influence the collector's performance.
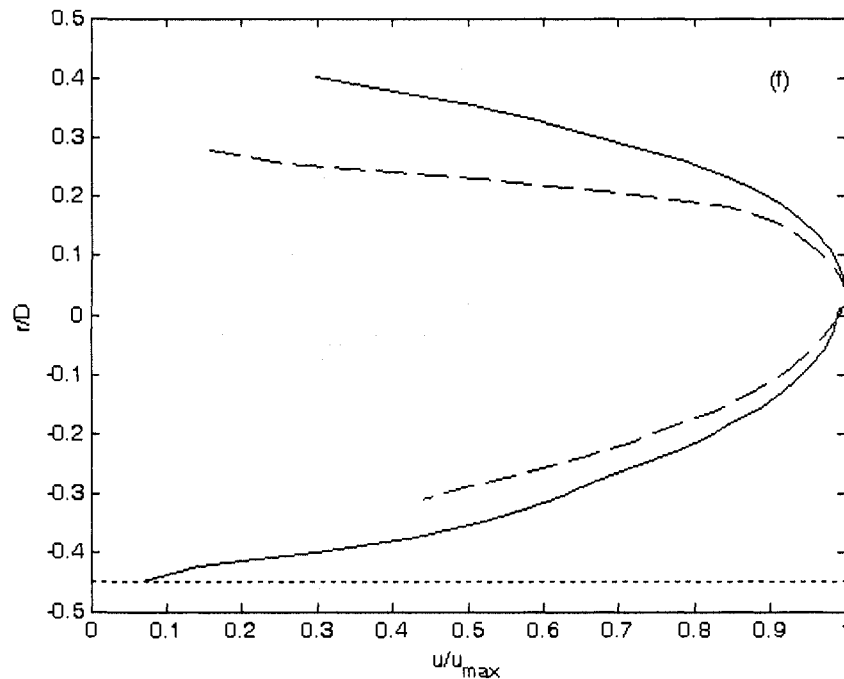
(b)

(c)

82
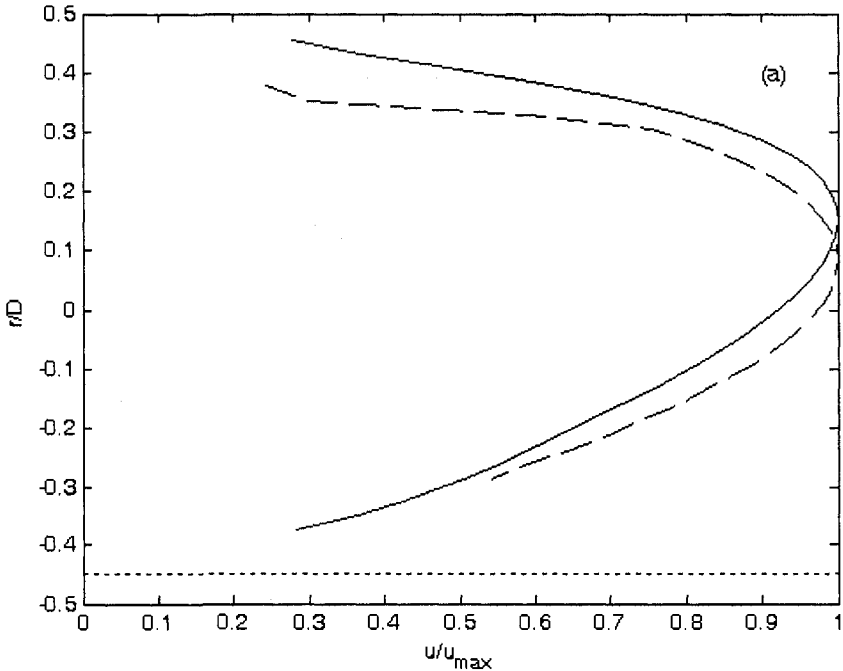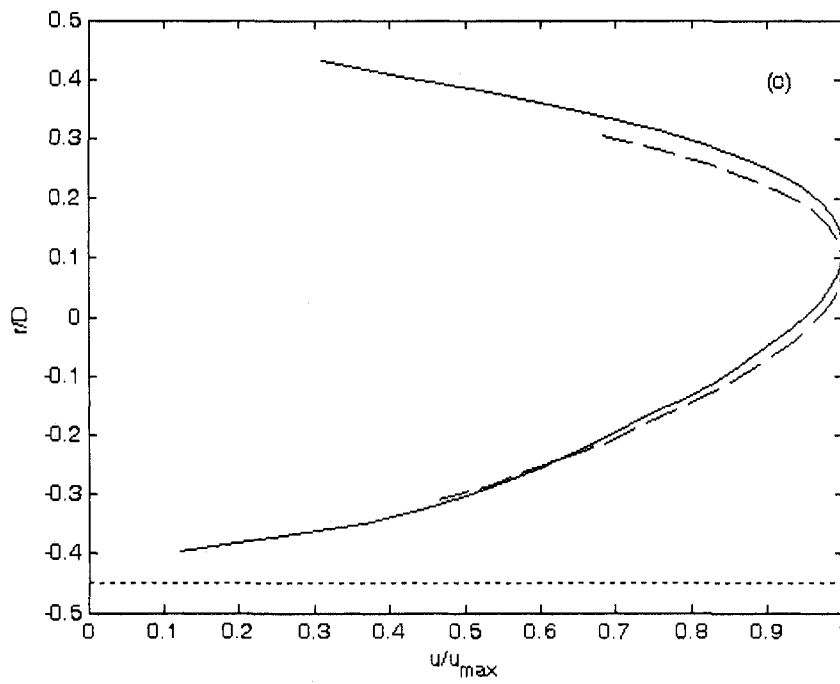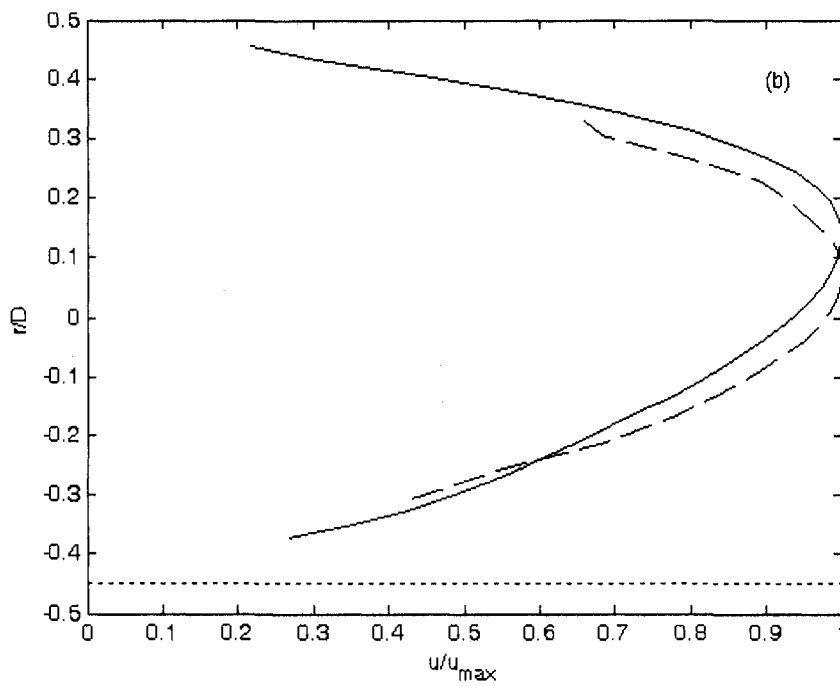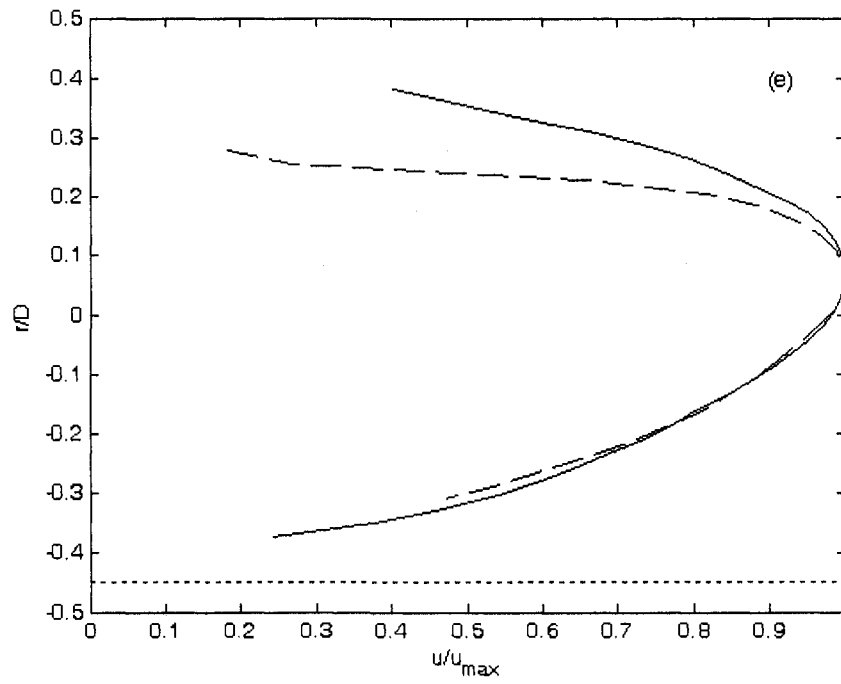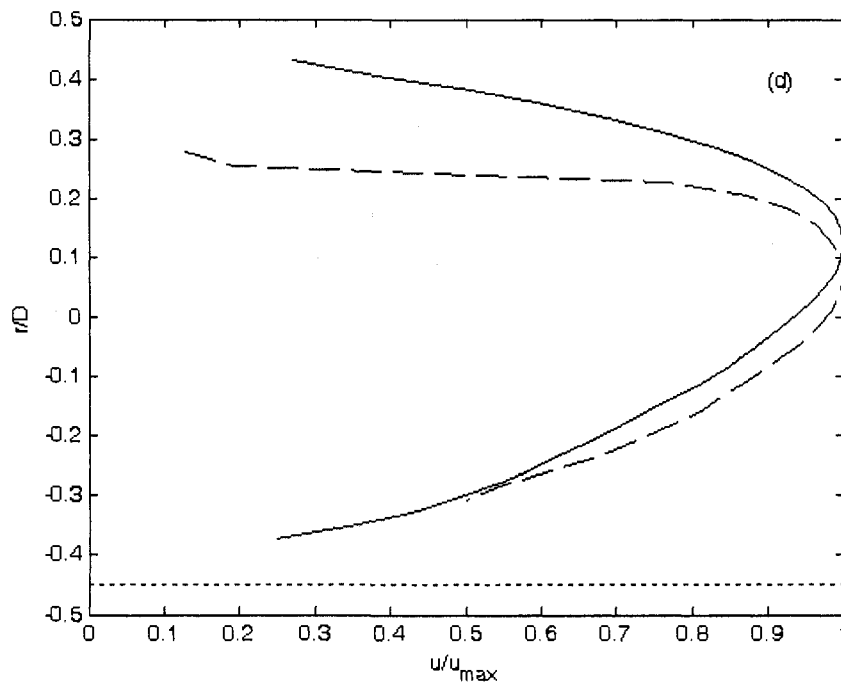
Figure 3.4: Non-dimensional unheated mean velocity profiles for two different pipe orientations. (a) Case I, (b) Case II, (c) Case III, (d) Case IV, (e) Case V, (f) Case VI. East-bounded (Solid Line), South-bounded (Dashed Line). The location of the plate-tube joint is shown with the dotted line.

3.3.2 Heated Collector

The velocity measurements for the heated collector were performed at the exit of the collector for the same flow rates as for the unheated condition and at heater surface temperatures of 300°C and 400°C. All experiments for the heated condition were performed with the north-south orientation of the collector. The mean velocity profiles for both heating conditions are plotted in Figures 3.5a to 3.5f for cases I to VI, respectively. The corresponding mean velocity profiles for the unheated condition are also plotted in the figures for comparison. Note that the case at the lowest flow rate at a heater surface temperature of 400°C was

omitted because water in the tube was evaporating which resulted in uncontrollable bubbles on the tube's surface which did not allow correct and reliable data to be obtained. This scenario is not realistic for solar water heating either.

The mean velocity profiles followed a similar trend. The velocity was generally higher for the 400°C case compared to the 300°C case. The shape of the profiles suggest that there is considerable buoyancy induced mixing for the heated condition. When the collector is heated, the peak velocity is shifted towards the bottom half of the tube. The results indicate that the location of the velocity peak is closer to the joint of collector plate and tube. Ouzzane and Galanis (2001) numerically showed that when a horizontal tube with an external longitudinal fin is heated from the top and insulated at the bottom, more heat is being transferred to the fluid in the bottom part of the tube compared to the top, after an initial entry length. The peak interfacial heat flux was found closer to the location of fin.
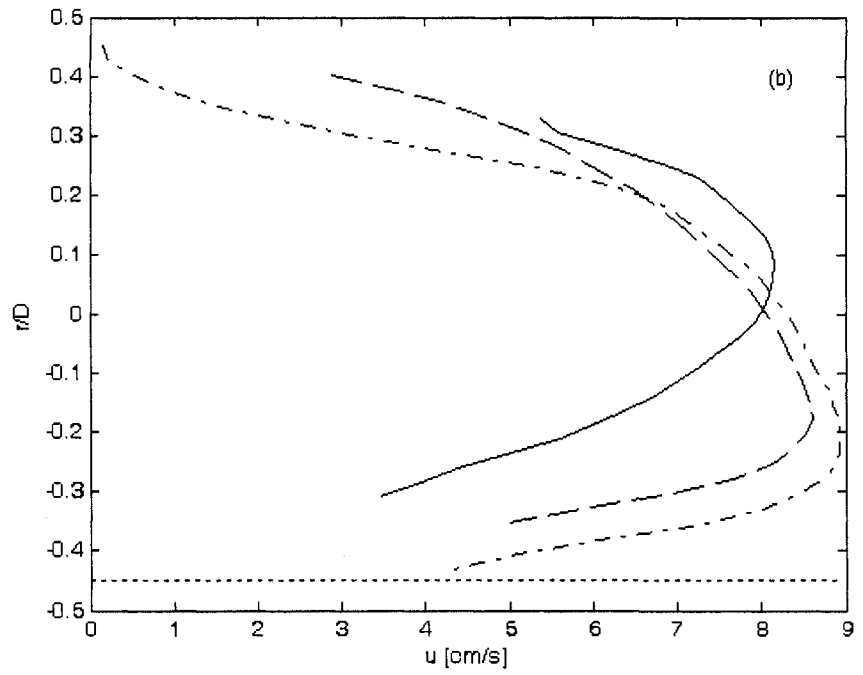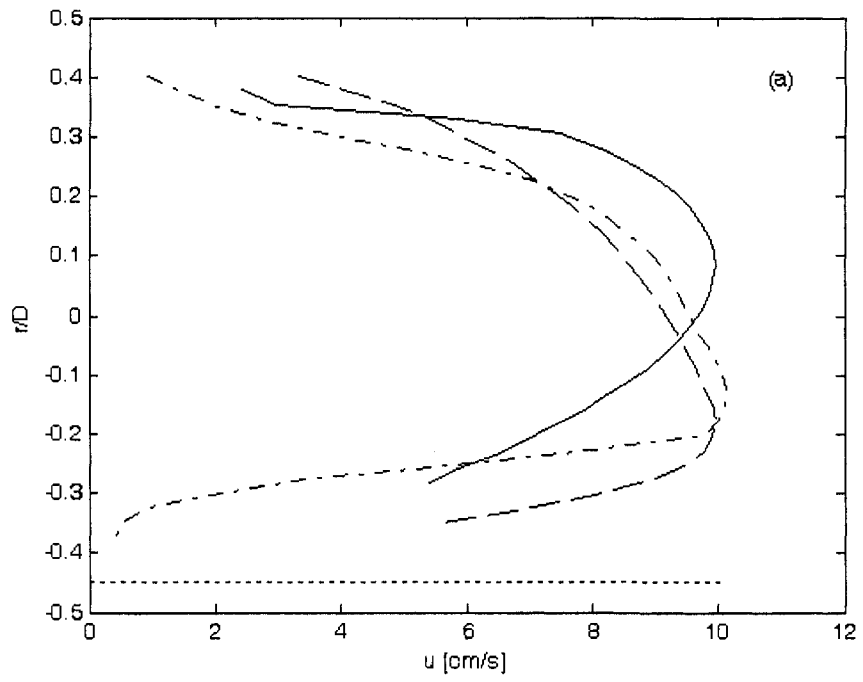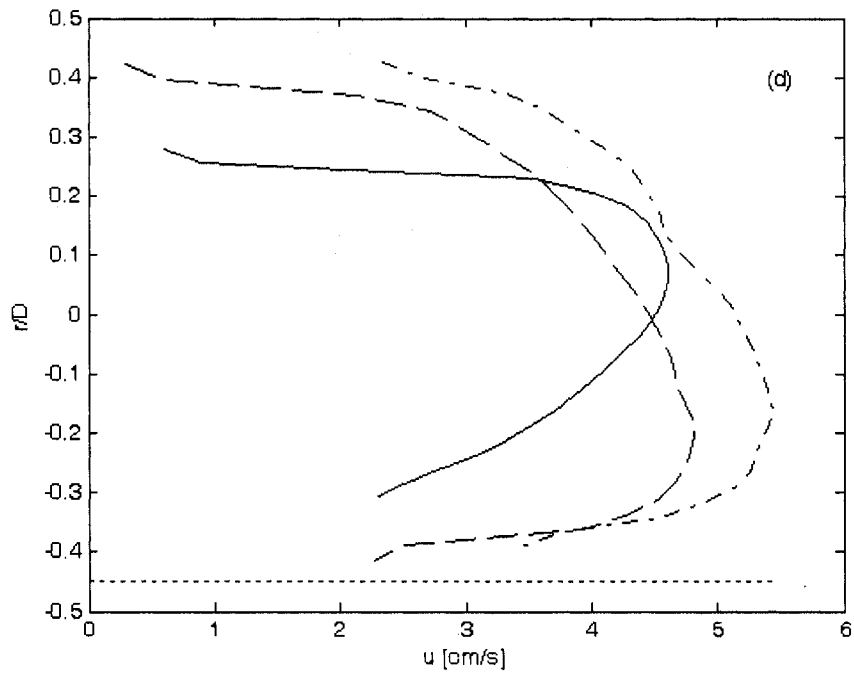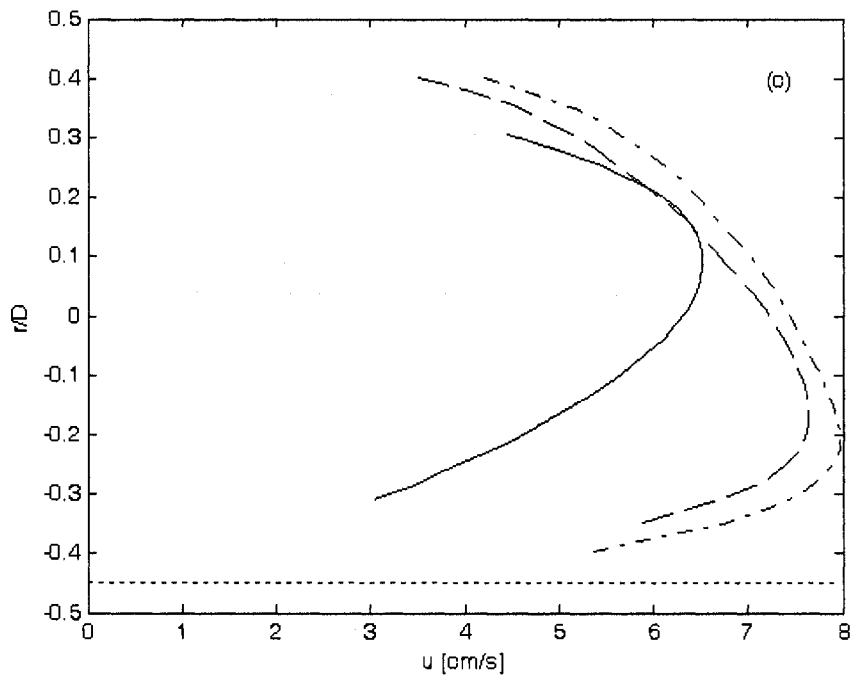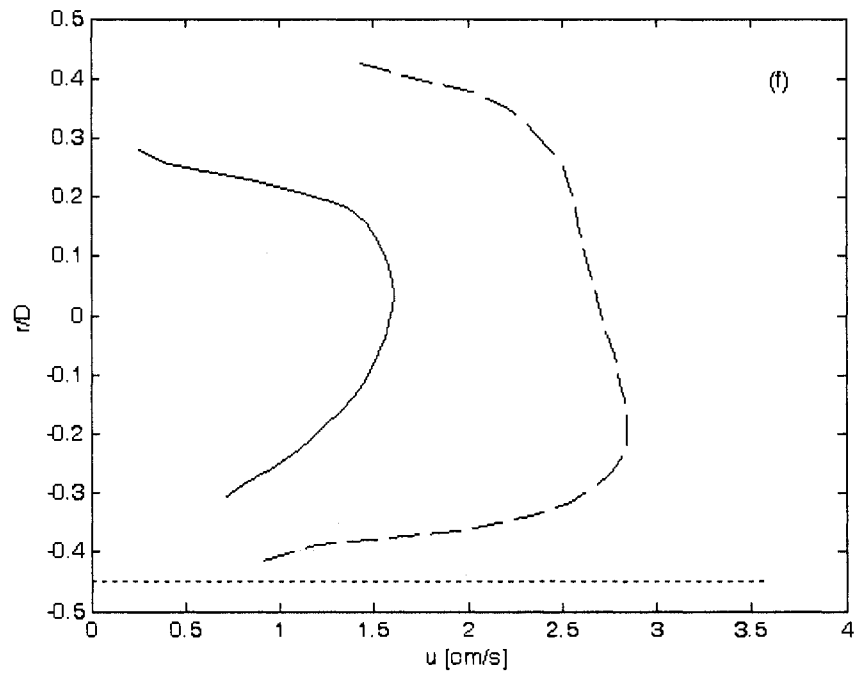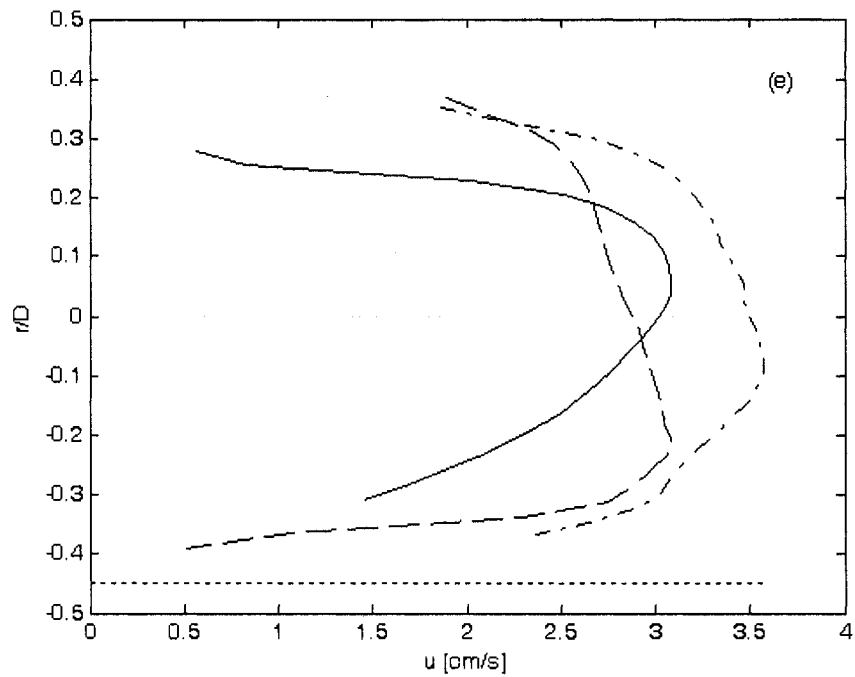
Figure 3.5: Mean velocity profiles for unheated and heated conditions. (a) Case I, (b) Case II, (c) Case III, (d) Case IV, (e) Case V, (f) Case VI. Unheated condition (Solid Line), heated condition at 300°C (Dashed Line), heated condition at 400°C (Dash-dotted line). The location of pipe-plate joint is shown with the dotted line.

When examined in sequence, Figures 3.5 (a) to (f) show the development of the flow over the length of the collector tube. Consider the non-dimensional axial location Z as given by:

$$Z = \frac{z}{D \, \text{Re} \, \text{Pr}}$$
(3.12)

where z is the axial location of the measurements, D, is the tube diameter, Re, is the Reynolds number, and Pr is the Prandtl number (Ouzzane and Galanis, 2001). The values of Z for the given cases are listed in Table 3.1.

Table 3.1: Non-Dimensional Length for the Two Heating Conditions

Case	Z	
	300°C	400°C
I	0.01399	0.01414
II	0.01748	0.01761
III	0.02212	0.02240
IV	0.03119	0.03186
V	0.04799	0.04861
VI	0.09824	XX

The results in Table 3.1 show that Z increases with the decrease in the flow rate. This indicates a longer development length at lower flow rates. The comparison of the changes in the general shape of the profile from high to low flow rates (Case I to VI) in sequence is similar to seeing how the flow develops along the tube. As an example, for Case VI, the flow would have had an axial velocity profile similar in shape to the first case close to the entrance. As the flow continues to move downstream, the velocity profiles will shift and adopt the profiles of the later cases until they have the shape of the fully developed profile. Awareness of how the shape changes may become important when developing mixing strategies because the fully-developed condition may not be reached in the flat plate collectors that are available commercially.

Table 3.2 shows the comparison of the peak velocity magnitudes for heated and unheated cases. The results show that at the higher heater surface temperature, the difference in the peak velocity magnitude between heated and unheated cases ranged from 1.82% to 18.17%. With ascending flow rate, the percent difference increased to a maximum (Case III) and then decreased. This suggests that the added energy (heat) is primarily used to accelerate the flow and little energy is used for mixing at the higher flow rates. At a lower flow rate, the reverse occurred. That is, more energy is being used to mix the fluid in the pipe. The 300°C heating case shows a similar trend where the difference in peak velocities ranged from -0.58% to 14.65%. At the lowest flow rate (Case VI), however, the difference in peak velocity was 43.44%. The cause of this large

difference is speculated to be due to Case VI being the only case where the secondary flow intensity reached the fully-developed condition upstream from where the measurements were taken. Ouzzane and Galanis (2001) presented the axial evolution of the secondary flow where they illustrated that the magnitude of the secondary flow velocity increases from the lowest at the tube entrance to a maximum at a downstream location and then reduces to the fully-developed condition at a location further downstream. In the first five cases, it is thought that the fully-developed region would require a longer collector. Considering that there is not any data for this flow rate at the 400°C heater temperature because the water started to evaporate, it is reasoned that Case VI reached fully-developed very early in the collector. Since it was fully-developed, the additional heating of the fluid until the measurement section caused the water to accelerate to a significantly higher velocity compared to the unheated condition.

Table 3.2: Comparison of Heated to Unheated Peak Velocities

Case	Percent Difference in Peak Velocity [%]	
	300°C	400°C
I	-0.58	1.82
II	5.35	8.29
III	14.65	18.17
IV	4.23	15.17
V	-0.23	13.01
VI	43.44	XX

The difference in peak velocity magnitude between the 300°C and 400°C cases at different flow rates are presented in Table 3.2. As expected, the velocities

were larger for the higher heating condition. The peak velocity magnitude increased with the decrease in the flow rate. It increased from 2.4% for Case I to 15.2% for Case V.

Table 3.3: Difference in Peak Velocities for the 300°C and 400°C Heating Conditions

Case	Nominal Difference [cm/s]	Percent Difference [%]
I	0.24	2.4
II	0.28	3.2
III	0.33	4.3
IV	0.62	12.9
V	0.47	15.2

3.4 Heat Transfer Analysis

As the above results indicate that the thermo-fluid behaviour inside the collector tube is complex which involves the superposition of buoyancy driven flow on the mean shear flow. Thus, the mode of heat transfer from collector's wall to the fluid is mixed convection which involves both forced and free convection. Therefore, it is important to quantify the contribution of forced and free convection modes to improve the understanding of the fundamental heat transfer process inside the collector.

The Grashof number represents the ratio of the buoyancy forces to the viscous forces acting on the fluid. Its role in free convection is analogous to the role that Reynolds number has in forced convection in determining the transition from

laminar to turbulent flow. The parameter Gr/Re^2 represents the ratio of buoyancy forces to inertial forces. It can be used to determine the relative importance of free convection. When $Gr/\mathrm{Re}^2 \approx 1$, free and force convection are of comparable magnitudes. If $Gr/\mathrm{Re}^2 \ll 1$, the forced convection is dominant. Free convection heat transfer is dominant when $Gr/\mathrm{Re}^2 \gg 1$. In this case, the Nusselt number is a function of the Grashof number and Prandtl number (Ozisik, 1985). The Grashof number was computed using Equation 3.6. The values of Grashof number for both heated conditions are presented in Figure 3.6 for cases I to VI. The Grashof numbers ranged between 3.25×10^6 and 8.14×10^6. The ratio Gr/Re^2 ranged from 3.57 to 162.44, indicating that free convection effects are dominant.
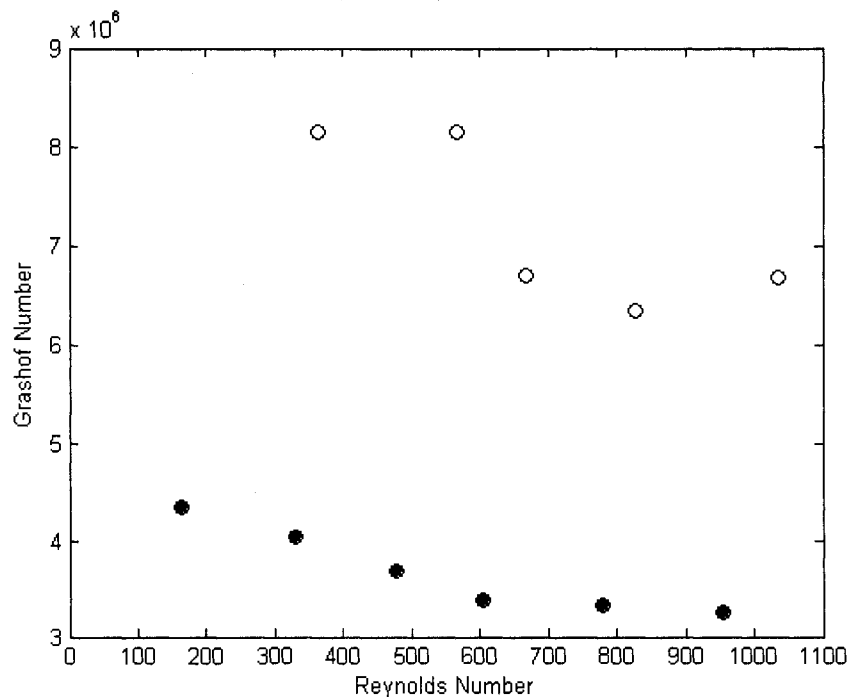

Figure 3.6: Grashof number versus Reynolds number for heater temperatures of 300°C (●) 400°C (○).

The Rayleigh number is a dimensionless parameter that relates buoyant and viscous forces acting on the fluid. When the Rayleigh number is sufficiently small, viscous forces are more dominant than the buoyancy forces and any disturbance due to the buoyancy are damped by the viscous forces. When the Rayleigh number exceeds a critical value of 1708, disturbances in the flow are not damped out but rather propagate and develop into a quasi-steady motion. The transition to fully turbulent free convection occurs when the Rayleigh number is of the order of 10^6. The Rayleigh number is calculated using Equation 3.9. The values of Rayleigh number for the two heat conditions are plotted in Figure 3.7. For both conditions, the Rayleigh number is of the order of 10^7 which confirm that the fluid inside the collector is undergoing turbulent free convection.
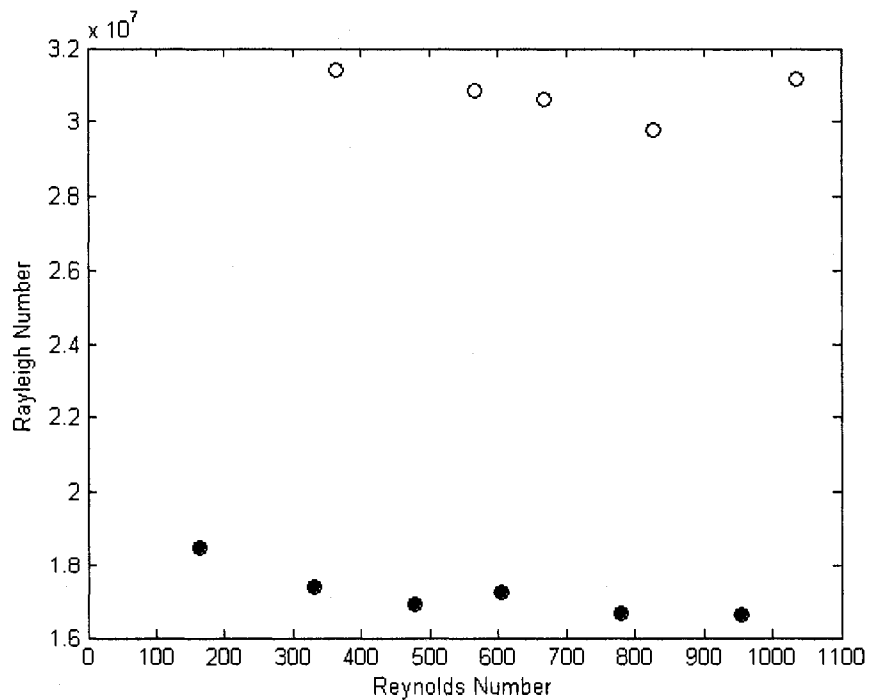

Figure 3.7: Rayleigh number versus Reynolds number for heater temperatures of 300°C (●) 400°C (○).

The Richardson number is another way to characterize the importance of buoyancy effects relative to inertia effects in a flow. It also quantifies the relative magnitudes of turbulence produced by buoyancy to the turbulence produced by the mean shear. It can be expressed as:

$$Ri = \frac{\Delta \rho}{\rho} \frac{gh}{u^2}$$ (3.13)

where ρ is the density, g is the gravitational constant, h is a characteristic length and u is the flow velocity (Cebeci, 1984). Typically, when $Ri \gg 1$, forced convection is negligible compared to natural convection. Calculated using Equation 3.10, the Richardson number is plotted against the Reynolds number in Figure 3.8. The result shows that as the Reynolds number decreased, Ri increased from approximately 4 to 160 at 400°C, and from approximately 6 to 60 at 300°C. It shows that in all cases, the buoyancy effects are dominant compared to the inertia forces. In other words, the turbulence produced by the mean shear is negligible and the main source of turbulence is buoyancy. If the buoyancy forces are stronger, the turbulence produced by the mean shear is utilized by working against the buoyancy forces (Turner, 1973). That is, buoyancy damps the shear produced turbulence. Hobbi (2007) studied the impact of heat enhancement devices on the performance of the flat-plate solar collector. He found no improvement in the performance of collector by inserting the heat enhancement devices. He concluded that due to the large values of Richardson number in the collector, turbulence produced by the mean shear was damped by

the strong buoyancy forces and thus, the heat enhancement devices which are based on enhancing the shear-produced turbulence are ineffective in solar collectors. The results in Figure 3.8 also show that the damping of shear-produced turbulence is very significant at lower flow rates.
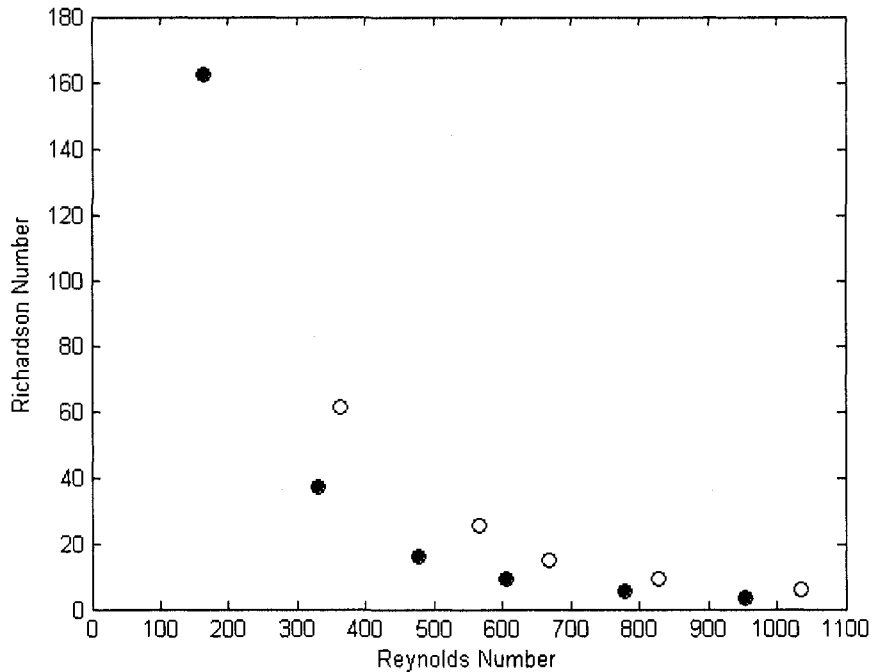

Figure 3.8: Richardson number versus Reynolds number for heater temperatures of 300°C (•) 400°C (o).

The Nusselt number represents the ratio of heat transfer by convection to heat transfer by conduction across a fluid layer. A Nusselt number of unity means that the heat transfer is purely through conduction. The Nusselt number is calculated using Equation 3.5. In Figure 3.9, the mean Nusselt number is plotted against Reynolds number for each experiment. It suggests that there is significant conduction between the fluid layers at the lowest flow rate. Unfortunately, since

the heat transfer problem in this work is unique, these results cannot be compared to other experimental studies. Other studies have dealt with similar geometry (horizontal pipes) but with different heating conditions (isothermally, uniform and non-uniform constant heat flux) or flow conditions (higher Reynolds numbers in the forced convection range).
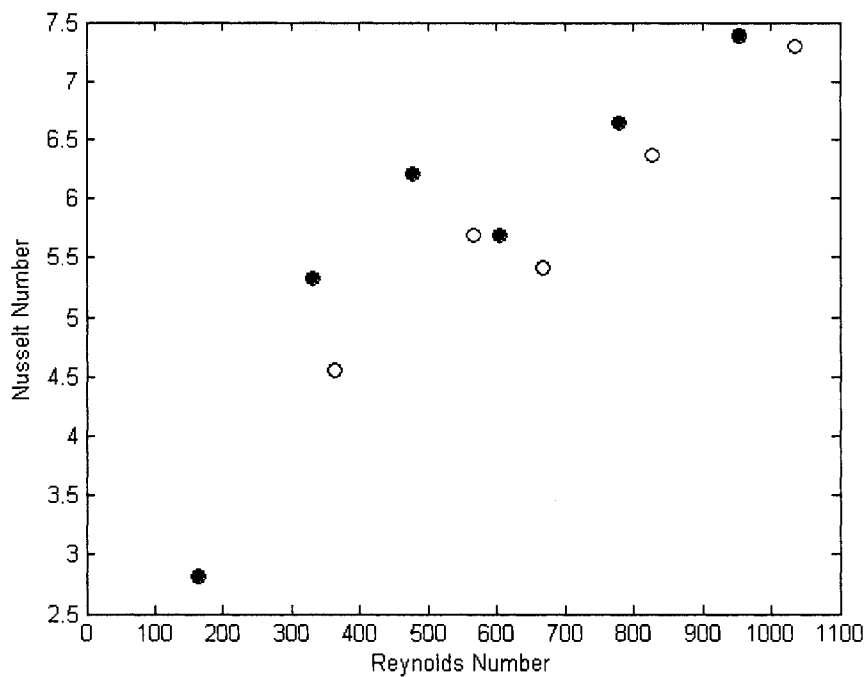

Figure 3.9: Nusselt number versus Reynolds number for heater temperatures of 300°C (●) 400°C (○).

3.5 Turbulent Velocity Characteristics

To find the turbulent characteristics for each experiment, the turbulent velocity fields were calculated. The turbulent velocity was calculated by subtracting the time-averaged mean velocity from the instantaneous velocity at each grid point.

The turbulent velocity data was then used to compute different turbulent properties. These properties were averaged at each location in the vertical plane along the radius of the tube. It must be noted that particle accumulation on the tube walls resulted in some data being unusable. Subsequently, the data near the walls in the profiles is missing.

The profiles of root-mean-square (RMS) horizontal turbulent velocity for cases I to VI are plotted in Figures 3.10 (a) to (f), respectively, for the heated and unheated conditions. Generally, the profiles increase to a peak near the tube walls and recede to a near-constant magnitude in the centre region. Again, due to the particle accumulation, this shape was not seen for all cases. Therefore, comparisons with respect to the location and magnitude of the peak cannot be made. The turbulent RMS velocity for 400°C heating condition tended to be larger in magnitude compared to the 300°C heating condition; the only exception is Case III. Similarly, the first and second cases are the only ones where the unheated condition had a larger magnitude than the 300°C condition. Only the unheated condition showed any possible relationship with respect to mass flow rate: magnitude increases with mass flow rate, but Case I did not fit this trend.

At the higher flow rate (Case I), the magnitude of horizontal turbulent velocity at 400°C is significantly large in the lower portion of the collector tube compared to other conditions, whereas the horizontal turbulent velocity magnitude in the upper portion of the tube is higher for the unheated condition. The velocity magnitude at

300°C is low and almost constant over the depth. The results for the unheated condition for Case II did not have a well pronounced constant region compared to the other unheated cases. There was more variation amongst the depths. As mentioned, Case III was the only case where the magnitude of the RMS horizontal turbulent velocity at the higher heating condition was less than the magnitude for the lower heating condition. Also, there are two other things noticed. First, the 300°C results showed a pronounced minimum near the tube centreline. The second observation is that the average magnitude in the constant region varied significantly for the three heating conditions. The other cases show similarity in magnitude for the centre region. It's only Case IV where this disparity is noticed again where the 400°C results are dramatically larger than the other two cases. At the lower flow rate (Case V), the profiles are similar for heated and unheated condition; however, the magnitudes are different. In Case VI, again, a definite minimum value is shown for the 300°C condition. Comparison of Figure 3.10 (a) and (e) shows that the magnitude of horizontal turbulent velocity in the upper and lower portions of the tube, decreased with the decrease in flow rate. This could be due to the reason that as the flow rate decreases, the buoyancy effects become more dominant and the turbulence is utilized in working against the buoyancy.
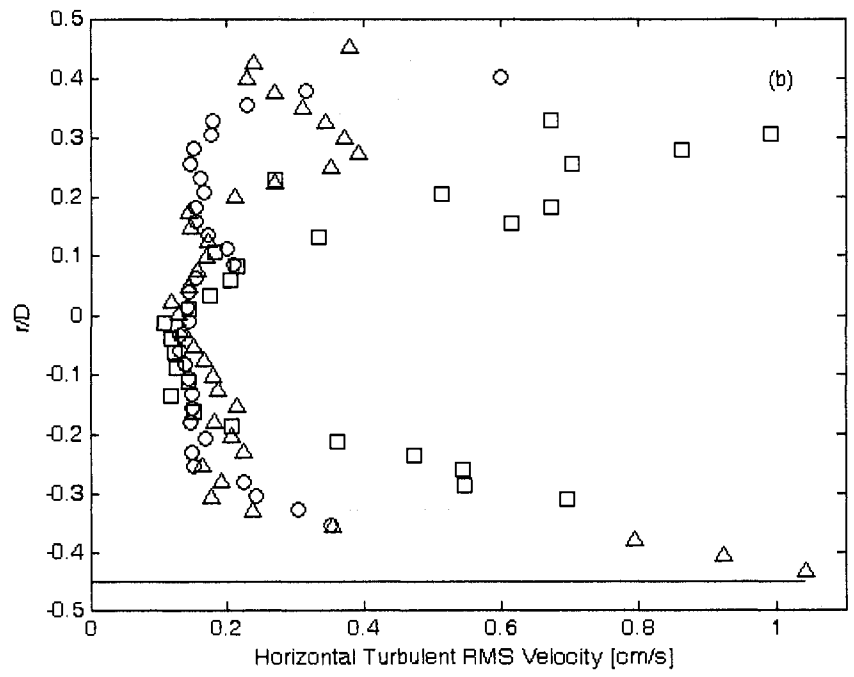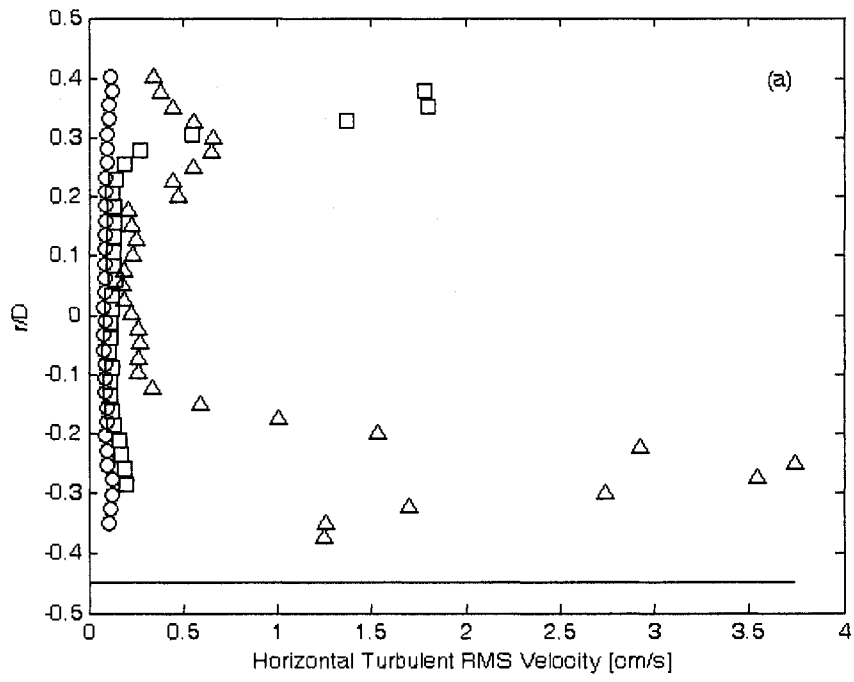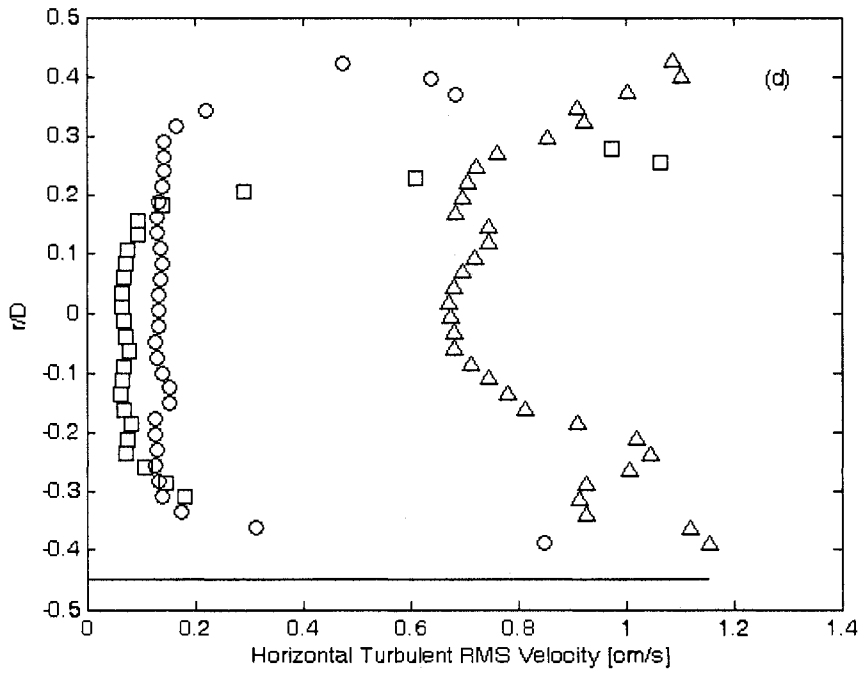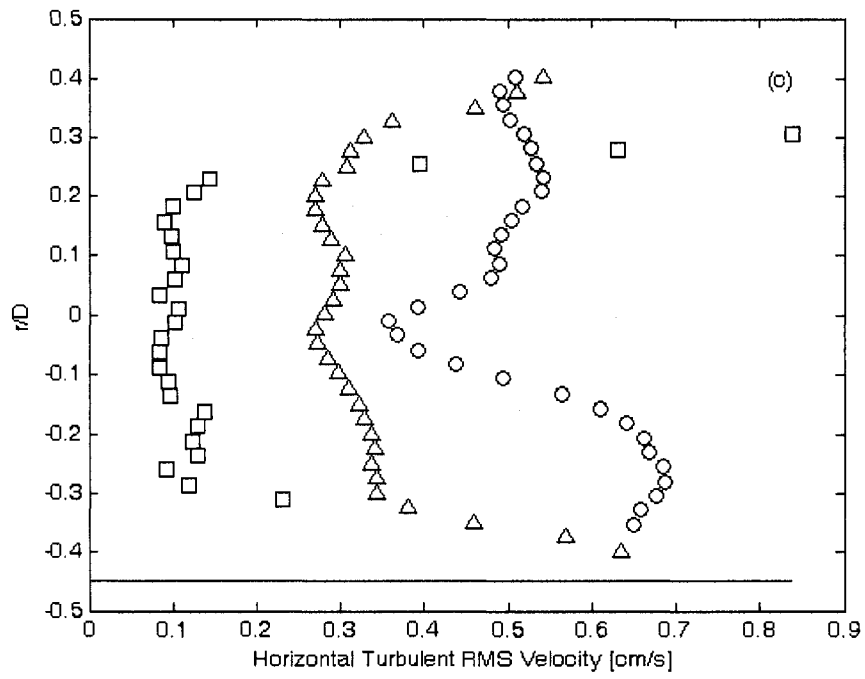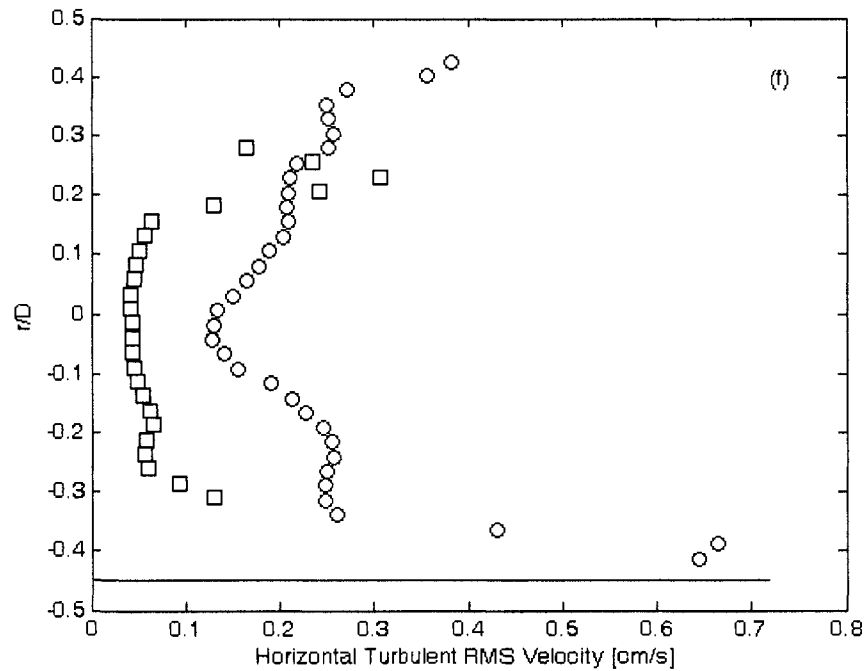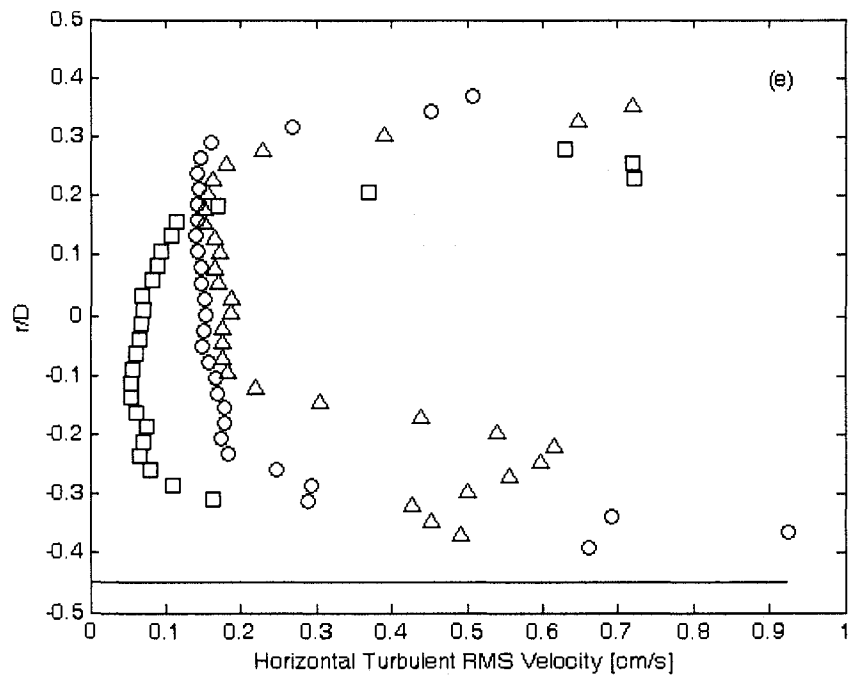
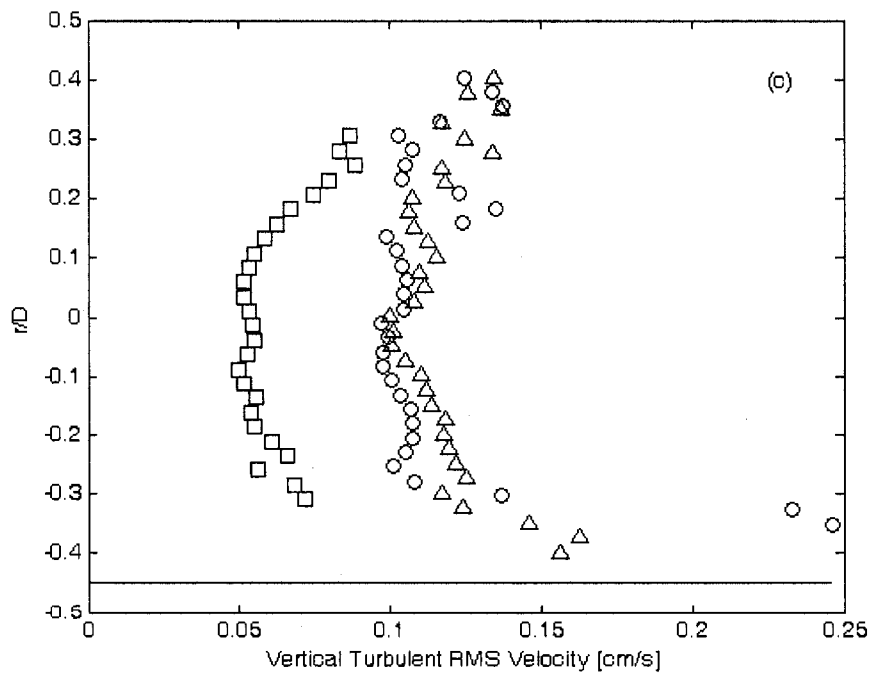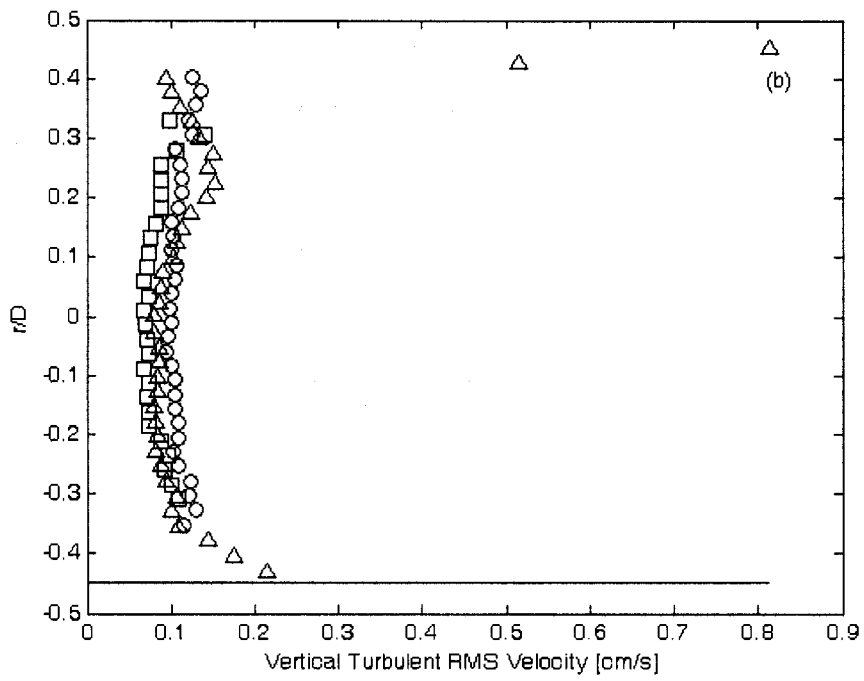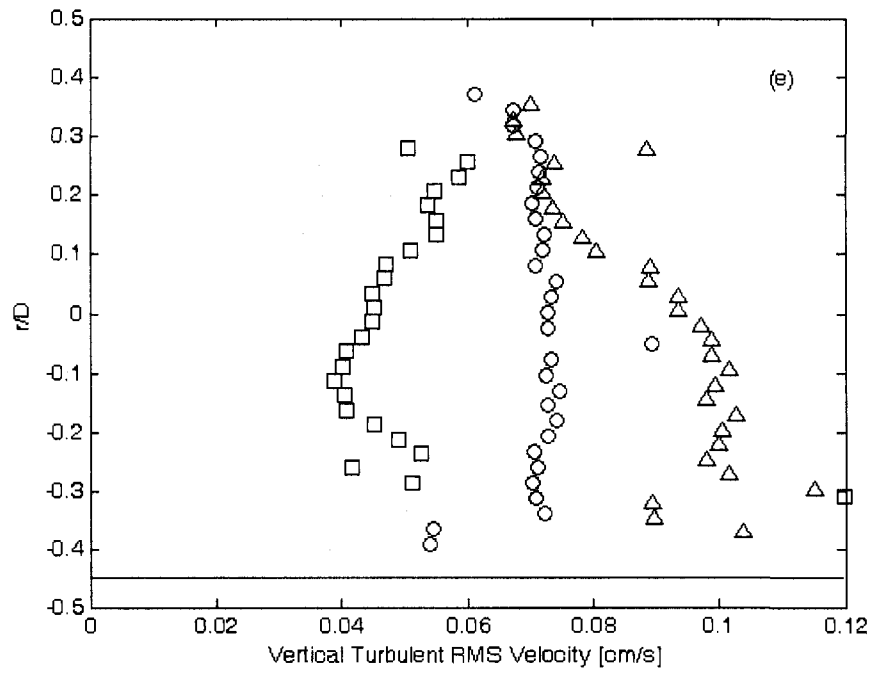Figure 3.10: The radial profiles of the RMS Horizontal Turbulent Velocity for the unheated and heated conditions. (a) Case I, (b) Case II, (c) Case III, (d) Case IV, (e) Case V, (f) Case VI. Unheated (□), 300°C (○), 400°C (△). The location of plate-tube joint is shown with the solid line.

102

The profiles of RMS vertical turbulent velocity are plotted in Figure 3.11 (a) through (f) for Cases I to VI, respectively, at the heated and unheated conditions. The profiles appear to have a similar shape as the horizontal RMS turbulent velocity where the peak magnitudes are observed near the tube walls and a near constant magnitude in the centre region of the cross-section. The magnitude of the RMS vertical velocity increased with the tube heating. In the centre region, the variation in magnitude along the depths was less than 1 cm/s for all cases, often much less. The vertical turbulent velocity fluctuations are expected to be lower in magnitude near the upper edge of the tube due to the formation of stably stratified layer. Due to the particle accumulation, no data is available but the profiles show a decreasing trend as they approach the upper layer.
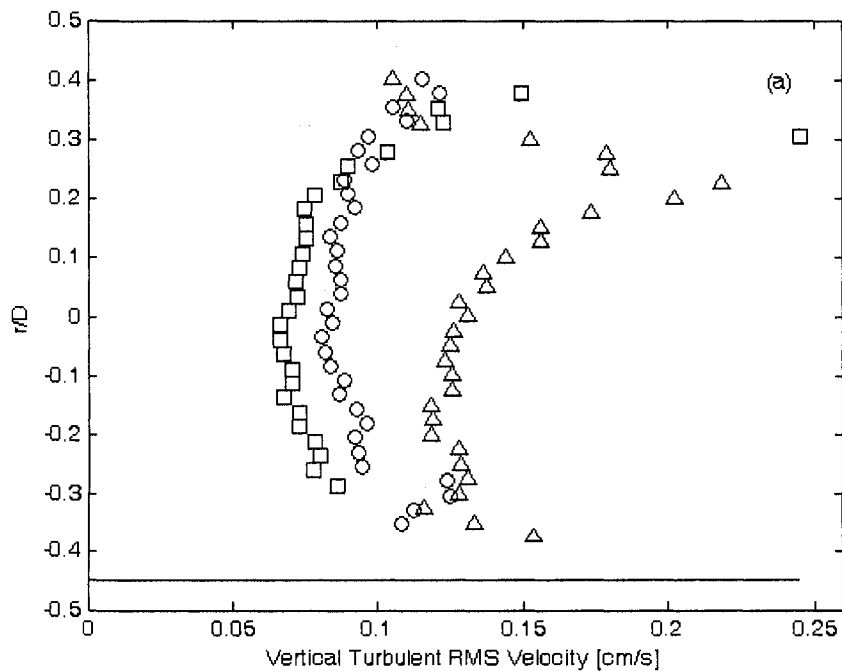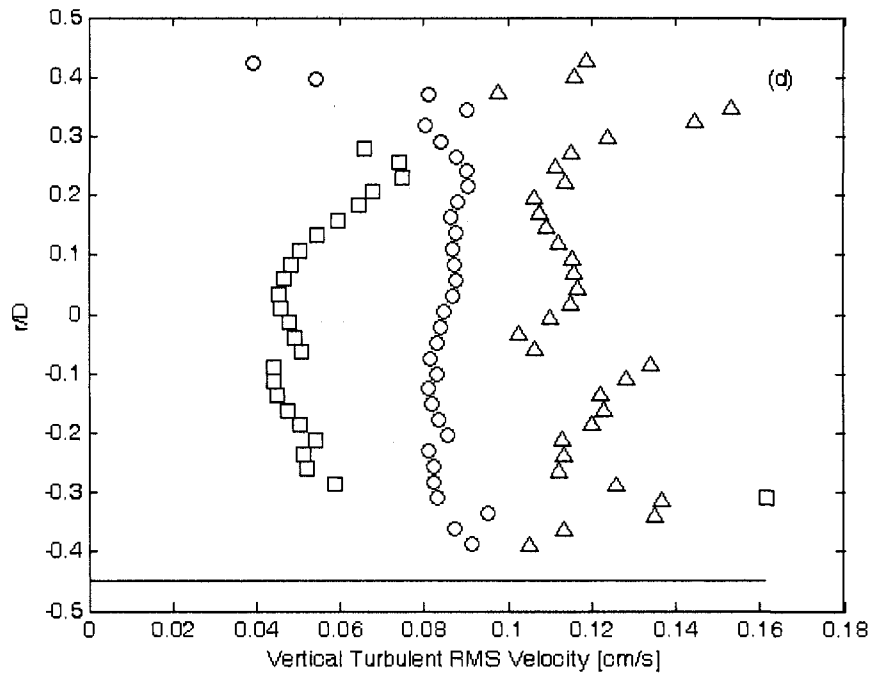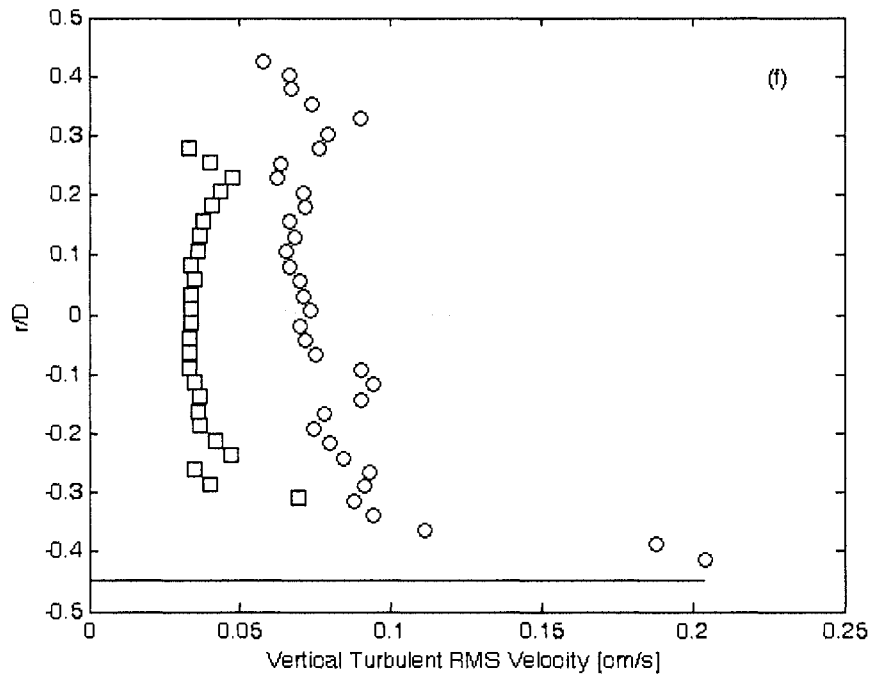
Figure 3.11: The radial profiles of the RMS Vertical Turbulent Velocity for the unheated and heated conditions. (a) Case I, (b) Case II, (c) Case III, (d) Case IV, (e) Case V, (f) Case VI. Unheated (□), 300°C (○), 400°C (△). The location of plate-tube joint is shown with the solid line.

Chapter 4 – Summary and Conclusion

Solar water heaters have tremendous potential in Canada. In addition to providing hot water for domestic applications, solar energy use reduces the dependence on conventional, non-renewable energy sources. However, more research must be conducted in order to improve their performance in cold climates. Also, individual components, like the collector, have not been studied in depth. Rather, the overall system design and performance have been given the most attention. The collector is a vital component of the solar water heating system because the actual energy conversion occurs inside of it. The work in this thesis examined the thermofluid behaviour within a flat-plate collector.

Two dimensional velocity fields were measured inside the collector tube using Particle Image Velocimetry (PIV) and temperature measurements were made using thermocouples. Special modifications have been made to the collector tube to allow optical access to enable PIV measurements. The measurements were performed for one unheated and two heated conditions at six flow rates that ranged from 0.00113 kg/s to 0.00781 kg/s. The results showed that the orientation of the collector tube with respect to the Earth's axis influences the overall flow behaviour inside the collector. While the shape of the mean axial velocity profile remained parabolic, the location of the maximum velocity changed with the orientation of the tube and stayed above the tube's centreline. The deviation of the peak from the centerline increased with the decrease in the Ekman number and was more significant at the higher flow rates. The present

results provide the first evidence that the Coriolis forces have a significant effect on low Reynolds number laminar flow in small diameter pipes. It was concluded that the orientation of collector tubes with respect to the flow direction would influence the flow behaviour inside the collector tube and could influence the collector's performance.

When the collector is heated, more heat to be transferred to the water in the lower portion of the tube because of the plate. Consequently, the peak velocity was in the bottom half of the tube because the axial component of the buoyancy force accelerates the water. As the water is heated, it rises along the tube wall as its density decreases. Eventually, a stably stratified layer in the upper portion of the tube is formed.

The circumferential wall temperature of the collector at the inlet, middle and outlet were measured during the experiments. The circumferential temperature distribution changes along the tube. At the inlet, the temperature at the plate-tube joint is higher due to the higher heat flux on the plate and circumferential heat conduction. At a downstream location, the temperature at the top of the tube overtakes the temperature at the joint which indicates the presence of a stably stratified region that reduces in the amount of heat transferred to the fluid in this region. Instead, heat is transferred circumferentially through conduction so that more heat reaches the bottom part of the tube, which always has the lowest temperature. The heat transfer analysis shows that free convection is the

dominant mode of heat transfer in the collector tube as indicated by the Richardson number ranging from 3.57 to 162.44. Rayleigh numbers on the order of 10^7 signify that there is turbulent free convection within the collector tube.

4.1 Future Work

This work is focused on the thermofluid behaviour within a flat-plate collector. With very little research available, a lot of work must be done in order to improve the understanding of the thermofluid behaviour inside the collector and to use this knowledge to improve their performance. Some specific issues that should be studied in future are described below:

- In the present experiments, the collector had a slight incline to help remove air bubbles. It is worth investigating the effect of an increase in the inclination angle on the thermofluid behaviour inside the collector. Specifically, determining if it would affect the stably stratified layer. The focus should be on collector angles that are used commercially.

- In the present experiments, the outside wall temperature of the collector tube was measured at three circumferential locations. To help understand the development of the stably stratified region, the temperature measurements inside of the tube at several spatial locations should be taken at different axial locations.

- The affect that the flow orientation has on the velocity profile for low Reynolds number laminar flow in tubes with small diameters needs to be further studied. Specifically, what impact that the Coriolis effects due to the Earth's rotation has on the flow behaviour inside the collector tube and whether it could be exploited to improve the collector's performance.

- Using the PIV technique, the effect of the heat transfer enhancement devices that Hobbi (2007) used can be investigated to further the understanding of their affect.

4.2 Contribution

The work of this thesis relates to the thermofluid behaviour within flat-plate collectors used for solar water heating. This is an area where very little work has been done previously. Most of the other studies are focussed on thermosyphonic systems which have limited potential in colder climates like Canada. There is little available regarding tubes heated non-uniformly from above with or without a longitudinal fin or a flat-plate. This work is specific in filling the current void of experimental work that focuses on the flow characteristics and wall temperature development along the length of the collector tube. The present study provided the first experimental measurements of the flow field inside a flat-plate solar collector tube. The impact of the radiant heating on the flow structure inside the flat-plate collector tube was also shown for the first time.

References

Aguilar, C. White, Ryan, D.J., & David L. (2005), "Domestic Water Heating and Water Heater Energy Consumption in Canada", Canadian Building Energy End-Use Data and Analysis Centre Report, CBEEDAC 2005-RP-02.

Antonopolous, K.A., & Rogdakis, E.D. (1991), "A Correlation for the Optimum Collector Flow Rate in One Tank Forced Circulation Solar Water Heaters", *Renewable Energy, 1 (3/4)*, 373 – 379.

Barozzi, G.S., Zanchini, E., & Mariotti, M. (1985), "Experimental Investigation Of Combined Forced and Free Convection in Horizontal and Inclined Tubes", *MECCANICA, 20*, 18 – 27.

Batchelor, G.K. (1967), *An introduction to fluid dynamics*, Cambridge University Press.

Behina, M., & Morrison, G.L. (1991), "An Experimental Investigation of Inclined Thermosyphons", *Solar Energy, 47(4)*, 313 – 326.

Benton, G.S. (1956), "The Effect of the Earth's Rotation on Laminar Flow in Pipes", *Transactions of the ASME, Journal of Applied Mechanics, 23*, 123 – 127.

Berman, A., Karn, R.K. & Epstein, M. (2006), "A New Catalyst System for High – Temperature Solar Reforming of Methane", *Energy & Fuels, 20*, 455 – 462.

Bojic, M., Kalogirou, S., & Petronijevic, K. (2002), "Simulation of a Solar Domestic Water Heating System Using a Time Marching Model", *Renewable Energy, 27*, 441 – 452.

Boone, Simon (n.d.), "Solar Energy in Canada: The Cost of Solar Water Heating", Retrieved October 10, 2008, from http://www.cansia.ca/Content/Documents/Document.ashx?DocId=12277

Carvalho, M.J., Collares-Pereira, M., Cunha, F.M., & Vitorino, C. (1988), An Experimental Comparison of Operating Strategies for Solar Water Systems", *Solar Energy, 41(1)*, 33 – 39.

Cebeci, Tuncer (1984), *Convective heat transfer (second revised edition)*, Long Beach: Horizons Publishing Inc.

Cowen, E.A. & Monismith, S.G. (1997), "A Hybrid Digital Particle Tracking Velocimetry Technique", *Experiments in Fluids, 22*, 199 – 211.

Draad, A.A. & Nieuwstadt, F.T.M. (1998), "The Earth's Rotation and Laminar Pipe Flow", *Journal of Fluid Mechanics, 361*, 297 – 308.

Duffie, John A. & Beckman, William A. (2006), *Solar engineering of thermal processes*. New York: John Wiley & Sons, Inc.

Fahmy, M.F.M., & Amd – El Sadek, M. (1990), "Transient Analysis of Closed Loop Solar Water Heating System (Effect of Heat Exchangers)", *Energy Conversion and Management, 30(4)*, 343 – 355.

Fanney, A. H. & Klein, S. A. (1988), "Thermal Performance Comparisons for Solar Hot Water Systems Subjected to Various Collector and Heat Exchanger Flow Rates", *Solar Energy, 40(1)*, 1 – 11.

Fincham A. M. & Spedding G.R. (1997), "Low cost, high resolution DPIV for measurement of turbulent fluid flow", *Experiments in Fluids, 23*, 449 – 462.

Fox, Robert W., McDonald, Allent T., & Pritchard, Philip J. (2004), *Introduction to fluid mechanics (sixth edition,)* New York: John Wiley and Sons.

Furbo, Simon & Mikkelson, Svend Erik (1987). Is low flow operation an advantage for solar heating systems?. In W. Bloss & F. Pfisterer (Ed.) *Proceedings of the Biennial Congress of the ISES, Germany* (pp. 962 – 966). New York: Pergamon Press.

112

Furbo, Simon, Vejan, Niels Kristian, & Shah, Louise Jivan (2005), "Thermal Performance of a Large Low Flow Solar Heating System with a Highly Thermally Stratified Tank", *Journal of Solar Energy Engineering, 127*, 15 – 20.

Gaa, F.O., Behina, M., & Morrison, G.L. (1996), "Experimental Study of Flow Rates Through Inclined Open Thermosyphons", *Solar Energy, 57(5)*, 401 – 408.

Gajusingh, Shivani Tara (2006), Influence of surface geometry and heating on the flow structure in wall-bounded flows. (Master's Thesis, Concordia University (Canada)).

Gordon, J.M.& Zarmi, Y. (1981), "Thermosyphon Systems: Single vs Multi-pass", *Solar Energy, 27(5)*, 441 – 442.

Habib, M.A., & Negm A.A.A. (2001), "Laminar Mixed Convection in Horizontal Concentric Annuli with Non-Uniform Circumferential Heating", *Heat and Mass Transfer, 37*, 427 – 435.

Health Canada (2004), "Canadian Handbook on Health Impact Assessment - Vol. 4: Health Impacts By Industry Sector", Retrieved October 10, 2008 from http://www.hc-sc.gc.ca/ewh-semt/pubs/eval/handbook-guide/vol_4/index-eng.php

Hobbi, A. (2007), Design of solar water heating systems for cold climate and study of heat transfer enhancement devices in flat-plate solar collectors. (Master's Thesis, Concordia University (Canada)).

Hollands, K.G.T. & Brunger, A.P. (1992), "Optimum Flow Rates in Solar Water Heating Systems with Counterflow Exchanger", *Solar Energy, 48(1)*, 15 – 19.

International Energy Agency (2006), World Energy Outlook 2006, Retrieved October 10, 2008, from http://www.worldenergyoutlook.org/2006.asp

Jesch, L.F. & Braun, J.E. (1984), "Variable Volume Storage and Stratified Storage for Improved Water Heater Performance", *Solar Energy, 33(1)*, 83 – 87.

Joudi, K.A., & Abd – Alzahra, H.A.A. (1984), "An Experimental Investigation into the Performance of a Domestic Forced Circulation Solar Water Heater Under Varying Operating Conditions", *Energy Conversion and Management, 24(4)*, 377 – 384.

Kalogirou, Soteris A. (2004), "Solar Thermal Collectors and Applications," *Progress in Energy and Combustion Science, 30*, 231 – 295.

Kennedy, J.B. & Neville, A.M. (1976), *Basic Statistical Methods for Engineers & Scientists*, New York: Harper & Row Publishers Inc.

Lawaetz, Henrik & Nielsen, Jan Erik (1987). Solar water heater with low flow. In W. Bloss & F. Pfisterer (Ed.) *Proceedings of the Biennial Congress of the ISES, Germany* (pp. 994 – 998). New York: Pergamon Press.

Mohammed, Hussein A. & Salman, Yasin K. (2007), "Free and Forced Convection Heat Transfer in the Thermal Entry Region for Laminar Flow Inside a Circular Cylinder Horizontally Oriented", *Energy Conversion and Management, 48*, 2185 – 2195.

Morrison, G.L & Braun, J.E. (1985), "System Modelling and Operation Characteristics of Thermosyphon Solar Water Heaters", *Solar Energy, 34(4/5)*, 389 – 405.

Morrison, G.L. Budihardjo, I., & Behina, M. (2004), "Water-in-Glass Evacuated Tube Solar Water Heaters, *Solar Energy, 76*, 135 – 140.

Morrison, G.L., Budihardjo, I. & Behina, M. (2005), "Measurement and Simulation of Flow Rate in a Water-in-Glass Evacuated Tube Solar Water Heater", *Solar Energy, 78*, 257 – 267.

Morrison, G.L. & Ranatunga, D.B.J. (1980), "Thermosyphon Circulation in Solar Collectors", *Solar Energy, 24(2)*, 191 – 198.

Natural Resources Canada (2003), "Solar Water Heating Systems A Buyer's Guide", Retrieved October 10, 2008, from http://www.canren.gc.ca/app/filerepository/SOLAR-BuyersGuide-SolarWaterHeatingSystems.pdf

Natural Resources Canada (2006), "Energy Use Data Handbook 1990 and 1998 to 2004", Retrieved October 10, 2008, from http://oee.nrcan.gc.ca/Publications/statistics/handbook06/index.cfm

Ouzzane, M. & Galanis, N. (1999), "Developing Mixed Convection in an Inclined Tube With Circumferentially Nonuniform Heating at its Outer Surface, *Numerical Heat Transfer, Part A: Applications, 35*, 609 – 628.

Ouzzane, M. & Galanis, N. (2001), "Numerical Analysis of Mixed Convection in Inclined Tubes with External Longitudinal Fins", Solar *Energy, 71(3)*, 199 – 211.

Ozisik, M. Necati (1985), *Heat transfer: A basic approach*, New York: McGraw – Hill.

Patankar, S.V., Ramadhyani, S. & Sparrow, E.M. (1978), "Effect of Circumferentially Nonuniform Heating on Laminar Combined Convection in a Horizontal Tube", *Journal of Heat Transfer, 100*, 63 – 70.

Phillips, W.F. (1981), "Effects of Stratification on the Performance of Solar Air Heating Systems", *Solar Energy, 26*, 175 – 180.

Phillips, W.F. & Dave, R.N. (1982), "Effects of Stratification on the Performance of Liquid-Based Solar Heating Systems", *Solar Energy, 29(2)*, 111 – 120.

Prasad A.K., Adrian R.J., Landreth C.C., & Offutt, P.W. (1992), "Effect of Resolution on the Speed and Accuracy of Particle Image Velocimetry Interrogation, *Experiments in Fluids, 13*, 105 – 116.

Robertson, H.S. & Patera, Russell P. (1982), "Collection of Solar Energy at Specified Output Temperature", *Solar Energy, 29(4)*, 331 – 337.

Shukla, S.N. & Tiwari, G.N. (1983), "Transient Analysis of Forced Circulation Solar Water Heating System with Collectors in Series", *Energy Conversion and Management, 23(2)*, 77 – 82.

Siddiqui, M. H. K., Loewen, M. R., Richardson, C., Asher, W.E. & Jessup, A.T. (2001), "Simultaneous Particle Image Velocimetry and Infrared Imagery of Microscale Breaking Waves", *Physics of Fluids, 13*, 1891 – 1903.

Siddiqui, Muhammad Husain Kamran (2002), Laboratory measurements of the flow beneath microscale breaking waves, (Ph. D Thesis, University of Toronto (Canada)).

Siegel, D.A. & Plueddemann, A.J. (1991), "The Motion of a Solid Sphere in an Oscillating Flow: An Evaluation of Remotely Sensed Doppler Velocity Estimates in the Sea", *Journal of Atmospheric Oceanic Technology, 8*, 296 – 304.

Sinha, S. & Tiwari, G.N. (1992), "Theoretical Evaluation of Commercial solar Hot Water System for Constant Delivery Temperature", *Energy Conversion and Management, 33(2)*, 125 – 133.

Sodha, M.S., Bapeshwara Rao, V.S.V., & Tiwari, G.N. (1983), "Performance of n Forced Circulation Water Heating Systems in Series", *Energy Research, 7*, 179 – 186.

Sodha, M.S., Shukla, S.N., Ranjan, V., & Tiwari, G.N. (1982a), "Transient Analysis of Forced Circulation Solar Water Heating System", *Energy Conversion and Management, 22*, 55 – 62.

Sodha, M.S., Shukla, S.N., Ranjan, V., & Tiwari, G.N. (1982b), "Transient Analysis of Closed Loop Solar Water Heating System", *Energy Conversion and Management, 22*, 155 – 161.

Snyder, W.H., & Lumley J.L. (1971), "Some Measurements of Particle Velocity Autocorrelation Functions in Turbulent Flow", *Journal of Fluid Mechanics, 48*, 41 – 71.

Turner, J.S. (1973), *Buoyancy effects in fluids,* Cambridge University Press.

Wuestling, M. D., Klein, S. A., & Duffie, J. A. (1985), "Promising Control Alternatives for Solar Water Heating Systems", *Journal of Solar Energy Engineering, 107,* 215 – 221.

van Koppen, C.W.J., Thomas, J.P. Simon, & Veltkamp, W.B. (1979), The actual benefits of thermally stratified storage in a small and medium size solar system. In K. Boer & B. Glenn (Ed.) *Proceedings of the ISES Silver Jubilee Congress, Atlanta* (pp. 576 – 580). New York: Pergamon Press.

Yadav, Y.P.,& Tiwari, G.N. (1988), "Parametric Studies of Tube in tube Heat Exchanger Coupled to a Panel of Collectors", *Energy Conversion Management, 28(1),* 81 – 93.